Cellular/Molecular

Beyond Glycolysis: Aldolase A Is a Novel Effector in Reelin-Mediated Dendritic Development

Gavin D. Lagani,[1] Mingqi Sha,[1] Weiwei Lin,[2,3] Sahana Natarajan,[1] Marcus Kankkunen,[1] Sabrina A. Kistler,[3] Noah Lampl,[2] Hannah Waxman,[1] Evelyn R. Harper,[1] Andrew Emili,[2] Uwe Beffert,[1] and Angela Ho[1]

[1]Department of Biology, Boston University, Boston, Massachusetts 02215, [2]Center for Network Systems Biology, Department of Biochemistry, Boston University Chobanian & Avedisian School of Medicine, Boston, Massachusetts 02118, and [3]Department of Pharmacology, Physiology & Biophysics, Boston University Chobanian & Avedisian School of Medicine, Boston, Massachusetts 02118

Reelin, a secreted glycoprotein, plays a crucial role in guiding neocortical neuronal migration, dendritic outgrowth and arborization, and synaptic plasticity in the adult brain. Reelin primarily operates through the canonical lipoprotein receptors apolipoprotein E receptor 2 (Apoer2) and very low-density lipoprotein receptor (Vldlr). Reelin also engages with noncanonical receptors and unidentified coreceptors; however, the effects of which are less understood. Using high-throughput tandem mass tag (TMT) liquid chromatography tandem mass spectrometry (LC-MS/MS)-based proteomics and gene set enrichment analysis (GSEA), we identified both shared and unique intracellular pathways activated by Reelin through its canonical and noncanonical signaling in primary murine neurons of either sex during dendritic growth and arborization. We observed pathway cross talk related to regulation of cytoskeleton, neuron projection development, protein transport, and actin filament-based process. We also found enriched gene sets exclusively by the noncanonical Reelin pathway including protein translation, mRNA metabolic process, and ribonucleoprotein complex biogenesis suggesting Reelin fine-tunes neuronal structure through distinct signaling pathways. A key discovery is the identification of aldolase A, a glycolytic enzyme and actin-binding protein, as a novel effector of Reelin signaling. Reelin induced de novo translation and mobilization of aldolase A from the actin cytoskeleton. We demonstrated that aldolase A is necessary for Reelin-mediated dendrite growth and arborization in primary murine neurons and mouse brain cortical neurons. Interestingly, the function of aldolase A in dendrite development is independent of its known role in glycolysis. Altogether, our findings provide new insights into the Reelin-dependent signaling pathways and effector proteins that are crucial for dendritic development.

Key words: actin; aldolase; cytoskeleton; dendrite; Reelin; signaling

Significance Statement

Reelin is an extracellular glycoprotein that exerts its function primarily by binding to the canonical lipoprotein receptors Apoer2 and Vldlr. Reelin is best known for its role in neuronal migration during prenatal brain development. Reelin also signals through a noncanonical pathway outside of Apoer2/Vldlr; however, these receptors and signal transduction pathways are less defined. Here, we examined Reelin's role during dendritic outgrowth in primary murine neurons and identified shared and distinct pathways activated by canonical and noncanonical Reelin signaling. We also found aldolase A as a novel effector of Reelin signaling that functions independently of its known metabolic role, highlighting Reelin's influence on neuronal structure and growth.

Received Jan. 11, 2024; revised July 23, 2024; accepted Aug. 26, 2024.

Author contributions: G.D.L., A.E., U.B., and A.H. designed research; G.D.L., M.S., S.N., M.K., S.A.K., N.L., H.W., and E.R.H. performed research; G.D.L., M.S., W.L., S.N., M.K., S.A.K., N.L., and H.W. analyzed data; G.D.L., U.B., and A.H. wrote the paper.

We thank Dr. Dean Tolan who provided suggestions for this work. This work was supported by the National Institute of Aging Grant AG059762 and the Harold and Margaret Southerland Alzheimer's Research Fund to U.B. and A.H.

The authors declare no competing financial interests.

Correspondence should be addressed to Angela Ho at aho1@bu.edu.

https://doi.org/10.1523/JNEUROSCI.0072-24.2024

Introduction

Reelin is a secreted glycoprotein important for mammalian brain development and synaptic function (Tissir and Goffinet, 2003; Jossin, 2020). The canonical Reelin signaling pathway through the apolipoprotein E receptor 2 (Apoer2) and very low-density lipoprotein receptor (Vldlr) is best known for its role in neuronal migration and positioning in cortical layering during prenatal brain development (Caviness, 1976; Pinto-Lord et al., 1982; D'Arcangelo et al., 1995; Curran and D'Arcangelo, 1998;

Trommsdorff et al., 1999). Upon Reelin binding, Apoer2/Vldlr receptor clustering triggers intracellular Dab1 phosphorylation by the Src-family tyrosine kinases that leads to the activation of multiple downstream signaling pathways including phosphatidylinositol-3-kinase (PI3K) signaling to promote cytoskeletal changes necessary for correct neuronal positioning, axon guidance, dendrite growth, and branching (Pinto Lord and Caviness, 1979; Rice et al., 1998; Hiesberger et al., 1999; Howell et al., 1999, 2000; Arnaud et al., 2003; Bock and Herz, 2003; Niu et al., 2004; Jossin and Goffinet, 2007; Matsuki et al., 2008; Leemhuis et al., 2010; Dillon et al., 2017). In the adult brain, Reelin signaling also promotes the maturation and stabilization of dendritic spines (Pappas et al., 2001; Niu et al., 2008; Rogers et al., 2011; Bosch et al., 2016), the primary sites of excitatory synaptic transmission and activity-dependent synaptic plasticity, where Reelin has been shown to enhance hippocampal LTP and modulate synaptic remodeling (Weeber et al., 2002; Beffert et al., 2005; Y. Chen et al., 2005; Rogers et al., 2011; Bal et al., 2013). Therefore, a loss of Reelin or disruption in the Reelin signaling pathway has been implicated in a wide range of human neurological disorders such as lissencephaly, ataxia, autism spectrum disorders, schizophrenia, bipolar disorder, epilepsy, and Alzheimer's disease (Impagnatiello et al., 1998; Guidotti et al., 2000; Hong et al., 2000; Perisco et al., 2001; Grayson et al., 2005).

Reelin also signals through a noncanonical pathway such as integrins and ephrin receptors which act to further fine-tune Reelin-dependent migration (Dulabon et al., 2000; Bouche et al., 2013; Lee et al., 2014; Kohno et al., 2020). As such, Reelin signaling is multifaceted and activates overlapping signaling pathways following Reelin binding to its cell surface receptors. However, most of these pathways are not well characterized. Here, we investigated the role of the PI3K pathway in Reelin signaling on cytoskeleton remodeling related to dendritic outgrowth and branching. We conducted an unbiased tandem mass tag (TMT) liquid chromatography tandem mass spectrometry (LC-MS/MS) proteomics screen to delineate canonical and noncanonical Reelin signaling and identified overlapping and distinct intracellular pathways in primary murine neurons during periods of robust neurite outgrowth. We observed pathway cross talk between the canonical and noncanonical Reelin signaling pathways related to regulation of cytoskeleton, neuron projection development, protein transport, and actin filament-based process. We demonstrate that Reelin signaling regulates actin dynamics in developing neurites and found aldolase A, a glycolytic enzyme and actin-binding protein, as a novel downstream effector in the Reelin pathway necessary for dendritic growth and arborization. Interestingly, the function of aldolase A on dendrite outgrowth is independent of its glycolytic function. These findings uncover novel aspects of Reelin signaling revealing a broader impact beyond the well known canonical pathways and the discovery of aldolase A as a novel Reelin effector in influencing neuronal structure and growth.

Materials and Methods

Mice. All animal use was approved by the Institutional Animal Care and Use Committee at Boston University, and methods were performed in accordance with relevant guidelines and regulations. Timed pregnant Crl:CD1 (ICR) dams (strain code, 022; RRID:IMSR_CRL:022) were purchased from Charles River Laboratories. Mice of either sex were used for all mouse studies.

Primary murine neuronal cultures. Primary cortical and hippocampal neurons were prepared from CD1 embryos of either sex at embryonic (E)16.5 and E18.5, respectively. Dissection of the mouse cortex includes hippocampal structures. Briefly, the cortex and the hippocampi were independently dissected from each individual embryo and dissociated with trypsin for 10 min at 37°C, triturated, and plated onto pretreated 100 mg/ml poly-L-lysine wells (Sigma-Aldrich, catalog #P2636-100MG) 24 h prior to plating. To ensure consistency between cultures, cell density of the single-cell suspension was determined using Trypan blue and a hemocytometer. Cortical neurons were plated at 7.5×10^5 cells/well (12-well plate), and hippocampal neurons were plated at 5×10^4 cells/well (24-well plate). Neurons were maintained in Neurobasal media (Thermo Fisher Scientific, catalog #21103049) supplemented with 2% (*v*/*v*) B27 (Thermo Fisher Scientific, catalog #17504044) and 0.5 mM glutamine (Thermo Fisher Scientific, catalog #25030081) in a humidified incubator with 5% CO_2 at 37°C.

Generation of recombinant Reelin and GST-RAP. Stably transfected HEK293 cells (ATCC, catalog #CRL-1573, RRID:CVCL_0045) expressing full-length murine Reelin were grown in T75 flasks in DMEM media and maintained at 37°C and 5% CO_2. At ∼70% confluency, the media was replaced with phenol red free Neurobasal media. Following 48 h, the media were collected and spun down at $500 \times g$ at 4°C for 5 min to pellet cellular debris and dead cells. The supernatant was collected and concentrated using an Amicon stirred ultrafiltration cell (Merck Millipore, catalog #5124) with a Biomax 100 kDa ultrafiltration molecular weight membrane (Merck Millipore, catalog #PBHK06210). The concentrated Reelin containing media was sterile filtered using a 0.45 µm syringe filter (Merck Millipore, catalog #SLHAM33SS), aliquoted, and stored at −80°C. Mock media were generated using control vector transfected HEK293 cells and collected in parallel to the Reelin conditioned media to ensure consistency between conditions. Reelin- and mock-conditioned supernatants were tested for their ability to stimulate Reelin-dependent phosphorylation of Dab1. pGEX-RAP was transformed into BL21 DE3 *E. coli*. A single, isolated, colony was inoculated in a 5 ml starter culture and subsequently grown into 300 ml of LB media and induced with 1 mM IPTG for 4 h at 37°C. Cultures were spun down at $10{,}000 \times g$ for 15 min at 4°C, and the pellet was snap frozen in liquid nitrogen and kept at −80°C for 15 min. Pellet was thawed and resuspended in 20 ml ice-cold phosphate–buffered saline (PBS) containing 3U Benzonase/mL, 1% Triton X-100, 1 mM 2-mercaptoethanol, 1 mM EDTA, 1 mg/ml lysozyme, 2 µg/ml aprotinin, 1 µg/ml pepstatin, and 1 µg/ml leupeptin. Resuspension was incubated at room temperature for 30 min on a nutator and centrifuged at $4{,}000 \times g$ for 30 min at 4°C. Supernatant was run through a glutathione affinity resin column under gravity flow, and GST-RAP was eluted with glutathione buffer containing 50 mM reduced glutathione and 50 mM Tris–HCL, pH 8.0, in PBS and sterile filtered.

Biochemical analysis and quantitative immunoblotting. For Reelin stimulation, primary murine cortical neurons were treated with 50 nM Reelin or mock control media at 3, 7, or 14 d in vitro (DIV) for 30 min. GST-RAP conditions were pretreated with 100 nM GST-RAP or GST for 2 h prior to Reelin treatment. For Dab1 immunoprecipitation (IP), neurons were lysed in IP buffer containing 10 mM Tris–HCL, pH 8.0, 1% Triton X-100, 150 mM NaCl, 1 mM EDTA, pH 8.0, 2 µg/ml aprotinin, 1 µg/ml pepstatin, 1 µg/ml leupeptin, and phosphatase inhibitor cocktail (Bimake, catalog #B15001). Cell lysates were incubated with precipitating antibody against Dab1 (mouse anti-Dab1 2721, 1:100, kindly provided by Dr. Joachim Herz) for 2 h at 4°C followed by overnight incubation with 20 µl of protein G Ultralink resin (Thermo Fisher Scientific, catalog #53128). The resins were washed with IP buffer, and precipitated proteins were eluted with reducing SDS sample buffer, boiling for 5 min and resolved by SDS-PAGE. For pathway inhibitor treatments, neurons were treated either with 50 µm LY294002 (Cell Signaling Technology, catalog #9901S), 200 nM rapamycin (Merck Millipore, catalog #553211) or DMSO vehicle control for 30 min prior to Reelin stimulation. Briefly, cells were rinsed with PBS and collected in RIPA buffer (150 mM NaCl, 1% NP-40, 0.5% sodium deoxycholate, 0.1% SDS, 50 mM Tris–HCL), pH 8.0, supplemented with protease and phosphatase inhibitors. For protein degradation experiment, DIV

7 neurons were treated with 50 μM MG132 (Sigma-Aldrich, catalog #M7449) for 4 h prior to 50 nM Reelin stimulation. For Western blotting, nitrocellulose membranes were blocked in a 1:1 solution of PBS and Intercept (PBS) blocking buffer (LI-COR Biosciences, catalog #927-70001) for 1 h at room temperature and incubated in primary antibodies overnight at 4°C. Primary antibodies used were mouse anti-Akt (Cell Signaling Technology, catalog #2920S; 1:2,000; RRID: AB_1147620), rabbit anti-Phospho-Akt Ser473 (Cell Signaling Technology, catalog #4060S; 1:2,000; RRID:AB_2315049), mouse anti-p70 S6 kinase alpha (Santa Cruz Biotechnology, catalog #sc-8418; 1:500; RRID:AB_628094), rabbit anti-Phospho-p70 S6 kinase Thr389 (Cell Signaling Technology, catalog #9205S; 1:1,000; RRID:AB_330944), mouse anti-GAPDH (Merck Millipore, catalog #MAB374; 1:2,000; RRID: AB_2107445), mouse anti-Dab1 (Santa Cruz Biotechnology, catalog #sc-271136; 1:500; RRID:AB_10610240), mouse anti-phosphotyrosine 4G10 (Merck Millipore, catalog #05-1050; 1:1,000; RRID:AB_916371), rabbit anti-aldolase A (Proteintech, catalog #11217-1-AP; 1:2,000; RRID: AB_2224626), and mouse anti-β-actin (Cell Signaling Technology, catalog #3700S; 1:2,000; RRID:AB_2242334). Membranes were washed and incubated in IRDye 800CW goat anti-mouse IgG (LI-COR Biosciences, catalog #926-32210; 1:20,000; RRID:AB_621842) and IRDye 680RD goat anti-rabbit IgG (LI-COR Biosciences, catalog #926-68071; 1:20,000; RRID: AB_10956166) for 1 h at room temperature and imaged using a LI-COR Biosciences Imaging Odyssey Clx System.

Digitonin permeabilization assay. Primary murine cortical neurons were briefly rinsed with ice-cold PBS and permeabilized with 150 μl of 30 μg/ml digitonin (Sigma-Aldrich, catalog #D141-100MG) in PBS for 5 min at 4°C. The supernatant was collected after incubation, and the cells were lysed with 200 μl RIPA buffer as stated above. Equal volumes of supernatant and lysate were run on 10% Tris-glycine SDS-PAGE, transferred to nitrocellulose membrane, and immunoblotted for rabbit anti-aldolase A (Proteintech, catalog #11217-1-AP; 1:2,000; RRID: AB_2224626) and mouse anti-β-actin (Cell Signaling Technology, catalog #3700S; 1:2,000; RRID:AB_2242334) overnight at 4°C.

Immunocytochemistry. Primary murine hippocampal neurons were cultured on 12 mm glass coverslips (Electron Microscopy Sciences, catalog #72222-01). DIV 7 neurons were treated with mock control, 50 nM Reelin, 100 nM GST-RAP for 2 h prior to Reelin, or 50 μM LY294002 for 30 min prior to Reelin stimulation (30 min). For the anisomycin experiment, DIV 7 neurons were treated with 40 μM anisomycin (Sigma-Aldrich, catalog #A9789) for 45 min prior to 50 nM Reelin stimulation. Cells were briefly rinsed with ice-cold PBS and fixed in 4% paraformaldehyde (PFA) for 10 min at room temperature. Cells were permeabilized in 0.1% Triton X-100 in PBS for 15 min and blocked in 5% normal goat serum in PBS for 1 h. For the α-tubulin immunocytochemistry, cells were permeabilized and blocked in 0.1% saponin and 10% normal goat serum for 30 min at room temperature. Primary antibodies used included mouse anti-β-actin (Cell Signaling Technology, catalog #3700S; 1:1,000; RRID:AB_2242334), mouse anti-β-actin (Proteintech, catalog #66009-1-Ig; 1:400; RRID: AB_2687938), mouse anti-α-tubulin (DM1A; Cell Signaling Technology, catalog #3873; 1:1,000; RRID:AB_1904178), rabbit anti-Phospho-Cofilin Ser3 (Cell Signaling Technology, catalog #3313S; 1:500; RRID: AB_2080597), or mouse anti-MAP2 (Merck Millipore, catalog #MAB3418; 1:2,000; RRID:AB_11212326). To selectively stain filamentous actin (F-actin), we used Alexa Fluor Plus 555 Phalloidin (Thermo Fisher Scientific, catalog #A30106; 1:400) in 5% goat serum in PBS for 1 h at room temperature. Following PBS washes, neurons were incubated with the fluorophore-conjugated secondary antibodies goat anti-rabbit IgG Alexa Fluor 488 (Thermo Fisher Scientific, catalog #A-11008; 1:500; RRID:AB_143165), goat anti-mouse IgG Alexa Fluor 488 (Thermo Fisher Scientific, catalog #A-11029; 1:500; RRID:AB_2534088), and goat anti-mouse IgG Alexa Fluor 546 (Thermo Fisher Scientific, catalog #A-11003; 1:500; RRID:AB_2534071) for 1 h at room temperature. Coverslips were mounted on SuperFrost Microscope Slides (Thermo Fisher Scientific, catalog #12-550-15) in ProLong Gold Antifade Mountant with DNA stain DAPI (Thermo Fisher Scientific, catalog #P36931).

Molecular cloning and lentivirus production. The shRNA construct for mouse aldolase A was generated using oligos directed toward the 3′-untranslated region (UTR) of *Aldoa* (GCCCACTGCCAATAAA CAACT) and control scrambled shRNA (CCGCAGGTATGCACG CGT) and cloned into the pLKO.1 cloning vector (Addgene, catalog #10878; RRID:Addgene_10878) and pCGLH vector for lentivirus and in utero electroporation (IUE) experiments, respectively. Additional shRNA constructs targeting mouse aldolase A were generated using two sets of oligos directed toward the open-reading frame (ORF) of *Aldoa* (A1, GCTGTGCCCAGTATAAGAA, and B2, GCTGCCAGT ATGTTACTGAGA) and cloned into pLKO.1 cloning vector for lentivirus experiments. To generate the lentiviral mouse R42A aldolase A mutant, we performed the site-directed mutagenesis with primer set (forward, CATTGCCAAGGCTCTGCAGTCCATTGG; reverse, CTTCCGG TGGACTCATCT) using the full-length mouse *Aldoa* cDNA (Sino Biological, catalog #MG52539-U) and Q5 Site-Directed Mutagenesis Kit (New England Biolabs, catalog #E0554S). Both aldolase A wild-type (WT) and R42A mutant were independently subcloned into pEGFP-C3 using primer set (forward, ACGGAATTCCAATGCCCCACCCATAC; reverse, CCAGGATCCTTAGTAGGCATGGTTAGAGATG) and subsequently subcloned into lentiviral pFUW vector using primer set (forward, ACGTCTAGAATGGTGAGCAAGGGCGAG; reverse, CCAGG ATCCTTAGTAGGCATGGTTAGAGATG). To generate the lentiviral mouse D33S aldolase A mutant, we performed site-directed mutagenesis with primer set (forward, GGCTGCATCTGAGTCCACCGGA; reverse, AGGATGCCCTTGCC) using the pFUW-EGFP-aldolase A WT construct and Q5 Site-Directed Mutagenesis Kit. Recombinant lentiviruses were produced by transfecting HEK293T cells (ATCC, catalog #CRL 3216; RRID: CVCL 0063) with pFUW plasmids for EGFP-aldolase A WT, EGFP-R42A aldolase A mutant, EGFP-D33S aldolase A mutant, or shRNA constructs with viral enzymes and envelope proteins (pMDLg/RRE, pRSV-REV, and pVSV-G) using FuGENE6 transfection reagent (Promega, catalog #E2692). HEK293T media were replaced with Neurobasal media (Thermo Fisher Scientific, catalog #21103049) supplemented with 2% (*v*/*v*) B27 (Thermo Fisher Scientific, catalog #17504044) 12 h after transfection, and the supernatant was collected 12 h after media change. Lentivirus-containing conditioned media were centrifuged at 500 × *g* for 5 min at 4°C to remove cellular debris and concentrated using Takara Lenti-X (Takara Bio, catalog #631231). Briefly, the supernatant was mixed with Lenti-X and incubated for 30 min at 4°C followed by centrifugation at 1,500 × *g* for 45 min at 4°C. The pellet was resuspended in 10% original volume in Neurobasal and stored at −80°C.

In utero electroporation. In utero electroporation (IUE) was performed on timed pregnant Crl:CD1 (ICR) dams (strain code, 022; RRID:IMSR_CRL:022) at E15.5 as described previously (Gal et al., 2006; Dillon et al., 2017). Dams were anesthetized with an intraperitoneal injection of a ketamine/xylazine mixture, and the uterine horns were exposed by midline laparotomy. One to two microliters of plasmid DNA (final concentration of 1 μg/μl) mixed with 0.25% fast green dye (Sigma-Aldrich, catalog #F7252) was injected into the lateral ventricles using a pulled glass micropipette. For electroporation, the anode of a Tweezertrode (Harvard Apparatus) was placed over the dorsal telencephalon above the uterine muscle, and four 36 mV pulses (50 ms pulse duration separated by 500 ms intervals) were applied with a BTX ECM830 pulse generator (Harvard Apparatus). Following electroporation, the uterine horns were returned to the abdominal cavity and filled with warm, sterile 0.9% saline. Absorbable sutures (Havel, catalog #HJ398) were used to close the abdomen, and nonabsorbable silk sutures (AD Surgical, catalog #M-S418R19) were used to stitch the skin above the abdominal wall. Dams were returned to a prewarmed clean cage and monitored closely during recovery.

Immunohistochemistry. Electroporated postnatal day (P)14 mice were anesthetized with an intraperitoneal injection of ketamine/xylazine and underwent transcardial perfusion with ice-cold 20 ml PBS followed by 20 ml ice-cold 4% PFA. Brains were removed and fixed in 4% PFA and 5% sucrose in PBS overnight at 4°C. Brains underwent cryoprotection

through a series of dehydration steps in 10, 20, and 30% sucrose in PBS. Brains were frozen in tissue molds with OCT compound and stored at −80°C. Coronal 40 µm brain sections were cut using a Leica CM1850 cryostat and mounted on SuperFrost microscope slides (Thermo Fisher Scientific, catalog #12-550-15) and stored at −80°C. Prior to immunostaining, sections were brought to room temperature in the dark and rehydrated using PBS and treated with 0.3% methanol peroxidase for 10 min to quench endogenous peroxidase activity. Antigen retrieval was performed by microwaving brain sections in 10 mM sodium citrate buffer, pH 6.0, at 900 W for 90 s followed by 100 W for 10 min. Sections were washed in PBS and blocked in 5% normal goat serum, 0.3% Triton X-100 in PBS for 1 h at room temperature followed by incubation with rabbit anti-GFP (Synaptic Systems, catalog #132 002; 1:500; RRID:AB_887725), mouse anti-SATB2 (Abcam, catalog #ab51502; 1:200; RRID:AB_882455) or mouse anti-Brn2 (Santa Cruz Biotechnology, catalog #sc-393324; 1:400; RRID:AB_2737347), and DAPI to distinguish cortical layers in 5% goat serum PBS overnight at 4°C. Sections were washed with PBS and incubated with goat anti-rabbit IgG Alexa Fluor 488 (Thermo Fisher Scientific, catalog #A-11008; 1:500; RRID:AB_143165) or goat anti-mouse IgG Alexa Fluor 546 (Thermo Fisher Scientific, catalog #A-11030; RRID:AB_2737024) for 1 h at room temperature before being mounted with ProLong Gold with DAPI.

Image acquisition and analysis. Images were captured using a Carl Zeiss LSM700 scanning confocal microscope with image acquisition settings kept constant between coverslips in independent experiments including settings for the laser gain and offset, scanning speed, and pinhole size. To determine fluorescence intensity in neurites from primary neuron cultures, we generated a maximum intensity projection image of the neuron through imaging the entire *Z*-stack of the neuron at 1 µm increments with a 40× oil objective. The regions of interest were selected manually in each image using well isolated neuronal processes. Selected neurites were straightened, and the pixel intensity was quantified using the National Institutes of Health (NIH) ImageJ software (http://imagej.nih.gov/ij). Experimenters were blind to conditions during image acquisition and analysis. For Sholl analysis, healthy, nonoverlapping neurons were chosen to minimize neurite crossover. Sholl analysis was conducted using the Neuroanatomy and NeuronJ plugins for ImageJ (Meijering et al., 2004). Concentric circles were spaced 10 µm apart starting from the center of the soma and extending to the end of the longest neurite. For Sholl analysis from IUE experiments, isolated GFP cell-filled neurons in primary somatosensory cortex (S1) were chosen. *Z*-stack images of selected neurons were acquired using a 25× oil objective and a 0.5 µm interval step. Full *Z*-stack images were 3D reconstructed using the Imaris image analysis software, and neuronal processes were manually traced to highlight the neuronal arborization pattern. Sholl analysis was conducted using concentric circles spaced 1 µm apart starting from the center of the soma and going to the end of the longest traced neurite. For apical neurite orientation, well isolated neurons in Layers 2/3 of S1 were chosen. Maximum intensity projection images were generated from *Z*-stack images of neurons taken with a 1 µm step interval using a 25× oil objective. Apical neurite orientation was determined using NIH ImageJ. A perpendicular line was drawn from the center of the soma to the pia, and a second line following the trajectory of the apical neurite was drawn starting at the soma. The angle between the two lines was used to determine neurite angle to the pia. Apical neurites were identified as the longest neurites originating at the apex of the soma with a trajectory of ≤90° to the pia. For layering and migration analysis, single plane images of cortical columns spanning the pia to the white matter in S1 were captured using a 25× oil objective. Using NIH ImageJ, boundaries between cortical layers were denoted, and the number of GFP-positive somas was counted in each layer. To determine the average distance from the pia, we drew a perpendicular line to the pia from the center of GFP labeled somas using NIH ImageJ.

LC-MS/MS. Primary murine cortical neurons were plated at 2×10^6 cells/well in six-well plates and treated with 50 nM Reelin, mock media control for 30 min, or 100 nM GST-RAP for 2 h prior to Reelin treatment at DIV 7. The media was aspirated and cells were briefly rinsed in ice-cold PBS and collected in 750 µl of ice-cold PBS and centrifuged at 500 × *g* for 2 min at 4°C. Cell pellets were snap frozen in liquid nitrogen and stored at −80°C. Samples were resuspended in 200 µl of GuHCL lysis buffer (6 M GuHCL, 100 mM Tris, 40 mM chloroacetamide, 10 mM TCEP), pH 8.0, with phosphatase inhibitor cocktail (Roche, catalog #4906837001) and EDTA-free protease inhibitor cocktail (Thermo Fisher Scientific, catalog #P190058) followed by heating to 95°C for 10 min. After brief sonication using a Branson probe sonicator with 10% power (40 kHz) for 10 s on ice to shear DNA, the samples were quantified via BCA assay (Thermo Fisher Scientific, catalog #23225). The samples were diluted with 100 mM Tris, pH 8.5, buffer to bring GuHCL concentration down to 0.75 M. Lysate proteins were digested with LC/MS-grade trypsin (1:50 enzyme to protein ratio, *w*/*w*) at 37°C overnight with shaking followed by the addition of formic acid (FA) to 1% in solution to terminate the trypsinization. The resulting peptides were desalted using a C18 solid-phase extraction (SPE) Sep-Pak column (Waters) as per the manufacturer's instructions. Briefly, after SPE columns were activated using 90% methanol and preconditioned using 0.1% TFA, the peptide digests were loaded, washed with buffer of 0.1% TFA two times and eluted with 0.1% TFA-60% acetonitrile. The desalted peptides were dried under vacuum at 45°C and kept at −20°C prior TMT labeling. Prior to TMT labeling, peptide quantification was performed by Pierce quantitative colorimetric assay (Thermo Fisher Scientific, catalog #P123275). Each sample comprising 100 µg peptides was incubated with TMTPro 16plex reagents (Thermo Fisher Scientific, catalog #A44520) as per the manufacturer's protocol. Reaction was carried out for 1 h at room temperature. To quench the reaction, we added 5% hydroxylamine to each sample and incubated for 15 min. Equal amounts of each sample were combined in a new tube, and a speed vac was used to dry the labeled peptide sample. The labeled peptides were desalted using a C18 SPE column. TMT-labeled peptides were then fractionated off-line on a Waters XBridge BEH C18 reversed-phase column (3.5 µm, 4.6 × 250 mm) using an Agilent 1100 HPLC system operated at a flow rate of 0.4 ml/min with two buffer lines: Buffer A (consisting of 0.1% ammonium hydroxide–2% acetonitrile-water) and Buffer B (consisting of 0.1% ammonium hydroxide–98% acetonitrile), pH 9. The peptides were separated by a gradient from 0 to 10% B in 5 min followed by linear increases to 30% B in 23 min, to 60% B in 7 min, and then 100% in 8 min and maintained at 100% for 5 min. This separation yielded 48 collected fractions that were subsequently combined into 12 fractions and evaporated to dryness in a vacuum concentrator. Fractions were kept at −20°C prior to LC-MS analysis. LC-MS analysis was performed using an Orbitrap Exploris 480 mass spectrometer equipped with FAIMS and interfaced to an Easy nanoLC1200 system (Thermo Fisher Scientific, catalog #LC140). Peptides were loaded onto a C18 precolumn (3 µm; 75 mm i.d. × 2 cm; 100 Å; Thermo Fisher Scientific, catalog #16-494-6) and then separated on a reverse-phase nanospray column (2 µm; 75 mm i.d. × 50 cm; 100 Å; Thermo Fisher Scientific, catalog #16-494-6) using gradient elution. Samples (~2 µg peptides) were injected and separated over 150 min gradient. The Mobile Phase A was consisted of 0.1% FA-2% acetonitrile, and Mobile Phase B was consisted of 0.1% FA-80% acetonitrile. The gradient consisted of 5–30% Mobile Phase B over 100 min, was increased to 60% Mobile Phase B over 20 min, and then was increased to 99% Mobile Phase B over 2 min and maintained at 95% Mobile Phase B for 5 min at a flow rate of 250 nl/min. The mass spectrometry instrument was operated in positive ion mode over a full mass scan range of m/z 350–1,400 at a resolution of 60,000 with a normalized AGC target of 300% for peptide. The source ion transfer tube temperature was set at 275°C and a spray voltage set to 2.5 kV. Data were acquired on a data-dependent mode with FAIMS running three compensation voltages at −50, −57, and −64 v. MS2 scans were performed at 45,000 resolution with a maximum injection time of 80 ms for peptides at normalized collision energy 34. Dynamic exclusion was enabled using a time window of 60 s.

Proteomic data analysis. MS2 spectra were processed and searched by MaxQuant (version 1.6) against a database containing the Uniprot mouse protein sequences (uniprot.org) and reversed (decoy) sequences for protein identification. The search allowed for two missed trypsin cleavage sites, variable modifications of methionine oxidation, and

N-terminal acetylation. The carbamidomethylation of cysteine residues was set as a fixed modification. Ion tolerances of 20 and 6 ppm were set for the first and second searches, respectively. The candidate peptide identifications were filtered assuming a 1% false discovery rate (FDR) threshold based on searching the reverse sequence database. Quantification was performed using the TMT reporter on MS2 (TMT pro16-plex). Bioinformatic analysis was performed in the R (version 4.3) statistical computing environment. Relative intensity of protein groups features was log2 transformed and then normalized by median method. The Limma R package was used for differential analysis (Ritchie et al., 2015) to generate ranked lists. The differential analysis and comparison between groups was performed using a Student's *t* test. Fast Gene Set Enrichment Analysis (Korotkevich et al., 2021) with statistical significance calculated using 10,000 permutations was used to identify biological terms, pathways, and processes that were coordinately up- and downregulated within each pairwise comparison. FDR cutoff was set to 0.05 for significant terms. Bar plots were generated with the ggplot Rpackage using the normalized enrichment score (NES). The mass spectrometry proteomics raw data have been deposited to the ProteomeXchange Consortium via the PRIDE repository with the dataset identifier PXD046667.

Quantification and data analysis. Experimenters were blind to condition during data acquisition and analysis. Statistical parameters are presented as mean ± SEM. To determine statistical significance between groups, we used unpaired *t* test to analyze all pairwise datasets and one- or two-way analysis of variance (ANOVA) for parametric analysis of multiple comparisons followed by Tukey's or Šídák's post hoc test. To determine the statistical significance of the Sholl analysis, we used a two-way ANOVA. Analysis was conducted using the Prism 8 software (GraphPad Software, RRID:SCR_000306). Significance was set to $p < 0.05$ for all experiments. Number of experiments and statistical information are reported on the corresponding result and figure legend sections.

Results

Reelin differentially activates PI3K/Akt and S6K1 phosphorylation across neuron development

We and others have shown when purified recombinant Reelin is added to murine cultured neurons, Reelin stimulates the phosphorylation of Dab1 and PI3K/Akt signaling pathways at DIV 3 (Beffert et al., 2002; Jossin and Goffinet, 2007; Leemhuis et al., 2010). Because Reelin signaling activates overlapping signaling pathways that govern important neuronal development and functions, including synaptic transmission, it is unclear whether Reelin activates the PI3K/Akt pathways uniformly throughout neuronal and synaptic development. To address this, we first stimulated primary murine cortical neurons, which also includes the hippocampus, with 50 nM Reelin or mock control at three developmental time points, DIV 3 (axon outgrowth), DIV 7 (dendritic outgrowth), and DIV 14 (mature synapses) for 30 min. We performed Dab1 IP to monitor Dab1 phosphorylation activity by immunoblotting with an anti-phosphotyrosine antibody and demonstrated Reelin consistently increased the levels of phosphorylated Dab1 in immunoprecipitates (Fig. 1*A–C*, Lane 2) compared with mock medium (Fig. 1*A–C*, Lane 1) at DIV 3, 7, and 14.

Next, we examined whether Reelin induces phosphorylation of Akt (Ser473) and S6K1 (Thr389) across all three neurodevelopmental time points. At DIV 3, we found a noticeable, although not significant, 49% increase in Akt phosphorylation following Reelin stimulation (Fig. 1*D,E*, Lane 2) compared with mock control (Fig. 1*D,E*, Lane 1). The 67% increase in Akt phosphorylation compared with mock control was insensitive to the downstream mTORC1 inhibitor rapamycin when neurons were treated 30 min prior to Reelin stimulation ($p = 0.0485$; Fig. 1*D,E*, Lane 4). As expected, Akt phosphorylation was prevented by inhibition of upstream PI3K with LY294002 (lanes 5 and 6, Fig. 1*D,E*). In addition, we observed a 160% increase in S6K1 phosphorylation after Reelin stimulation when compared with the mock control ($p = 0.0254$; Fig. 1*D,F*, Lane 2) at DIV 3, and this effect was inhibited by both rapamycin and LY294002 (Fig. 1*D,F*, Lanes 3–6). Likewise, at DIV 7, we observed Akt phosphorylation was increased by 59% after Reelin stimulation compared with the mock control ($p = 0.0412$; Fig. 1*G,H*, Lane 2) and increased to 77% in the presence of rapamycin ($p = 0.0071$; Fig. 1*G,H*, Lane 4) but was inhibited by PI3K inhibitor LY294002. Reelin stimulation led to a 46% increase in S6K1 phosphorylation when compared with the mock control at DIV 7 ($p = 0.0232$; Fig. 1*G,I*, Lane 2). By DIV 14, we did not observe any changes in both Akt and S6K1 phosphorylation following Reelin stimulation compared with the mock control (Fig. 1*J–L*). These results indicate that Reelin selectively activates S6K1 phosphorylation through the PI3K/Akt and the mTORC1 complex pathway during early axonal and dendritic outgrowth but not in mature neurons.

GSEA support roles of Reelin in regulation of cytoskeleton development and organization particularly related to actin filament-based process

Since we established Reelin activates the PI3K/Akt and mTORC1 signaling pathway during early neuronal development, we next wanted to elucidate the proteomic changes induced by Reelin stimulation during dendritic outgrowth at DIV 7, a period where we observed consistent PI3K/Akt and S6K1 phosphorylation. A preliminary time course in primary murine cortical neurons at DIV 7 demonstrated Reelin exerted a prominent effect on the proteome at 30 min compared with 3, 6, or 24 h using label-free quantification mass spectrometry (Extended Data Fig. 2-1). To examine the proteomic changes more extensively at 30 min, we treated DIV 7 primary murine cortical neurons in quadruplicates with four different conditions, mock control, 50 nM Reelin, 100 nM GST-RAP, or Reelin and GST-RAP, and performed LC-MS/MS analysis. RAP is a chaperone protein that acts in the secretory pathway to prevent premature binding of ligands to lipoprotein receptors prior to their insertion into the cell membrane (Bu and Rennke, 1996; Willnow et al., 1996). As such, RAP inhibits the canonical Reelin signaling pathway by preventing Reelin from binding to Apoer2 and Vldlr and blocking the Reelin-induced phosphorylation of Dab1 in primary neurons (Hiesberger et al., 1999). Indeed, we demonstrated that GST-RAP effectively blocked Reelin-induced Dab1 phosphorylation when primary murine cortical neurons were treated with 100 nM GST-RAP 2 h prior to Reelin stimulation at DIV 7 (Extended Data Fig. 2-2). With this experimental design, we can detect the following proteomic changes induced by Reelin: (1) canonical Reelin signaling by comparing the Reelin-treated group with the Reelin- and RAP-treated group where the difference represents the effect of Reelin signaling via the canonical receptors, Apoer2 and Vldlr which are inhibited by RAP; (2) noncanonical Reelin signaling by comparing the Reelin- and RAP-treated group with RAP alone where both groups are inhibited from interacting with the canonical receptors by RAP, so any difference between these groups would primarily be due to signaling via noncanonical receptors; (3) total Reelin signaling that includes both canonical and noncanonical signaling by comparing the Reelin-treated group with the mock control group where the difference represents the total effect of Reelin regardless of whether the signaling is by canonical or noncanonical receptors.

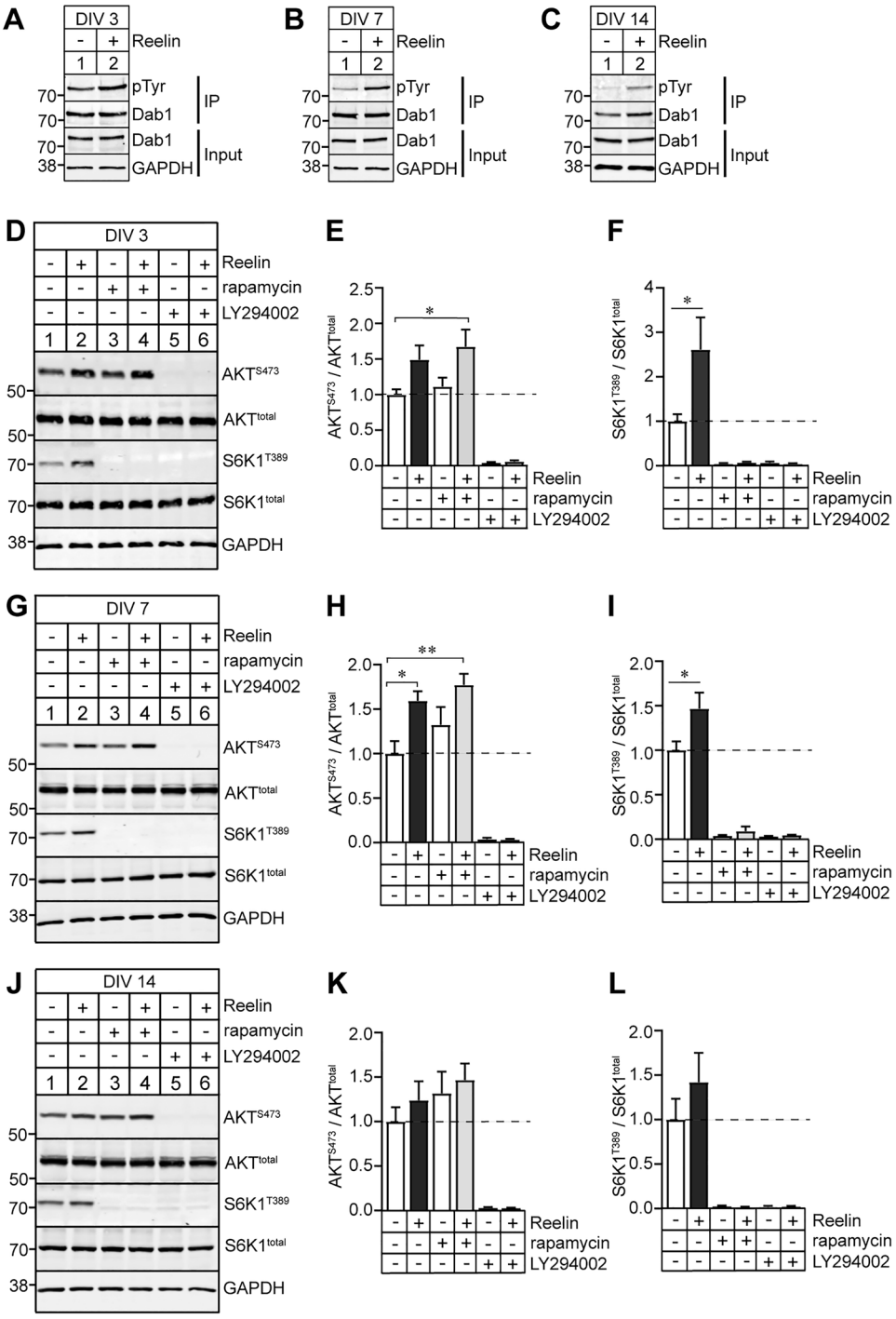

Figure 1. Reelin selectively activates the PI3K/Akt and S6K1 pathway in primary murine neurons at early developmental time points. ***A–C***, Representative immunoblots showing phosphotyrosine levels after Dab1 IP from primary murine cortical neurons treated with 50 nM Reelin or mock control for 30 min at DIV 3, 7, and 14. Total Dab1 and GAPDH serve as loading controls (input). ***D***, Representative immunoblots from DIV 3 neuronal lysates stimulated for 30 min with mock control (Lanes 1, 3, 5) or with 50 nM Reelin (Lanes 2, 4, 6). DIV 3 neuronal cultures were also incubated with 200 nM rapamycin (Lanes 3, 4) or 50 µM LY294002 (Lanes 5, 6) 30 min prior to Reelin stimulation. Cell lysates were immunoblotted for phosphorylated S473 Akt, total Akt, phosphorylated T389 S6K1, total S6K1, and GAPDH that serves as loading control. ***E***, Bar graph quantification for the ratio of phosphorylated S473 Akt with total Akt from ***D*** shows an increase in Akt phosphorylation following Reelin stimulation that was inhibited by LY294002 (one-way ANOVA; $F_{(5,\ 12)} = 24.55$; $p < 0.0001$). ***F***, Bar graph quantification for the ratio of phosphorylated T389 S6K1 with total S6K1 from ***D*** shows an increase in S6K1 phosphorylation following Reelin stimulation that was inhibited by rapamycin and LY294002 (one-way ANOVA; $F_{(5,12)} = 11.71$; $p = 0.0003$). ***G***, Representative immunoblots from DIV 7 neuronal lysates with the same treatment conditions as described in ***D***. ***H***, Bar graph quantification for the ratio of phosphorylated S473 Akt with total Akt from ***G*** (one-way ANOVA; $F_{(5,\ 12)} = 39.74$; $p < 0.0001$). ***I***, Bar graph quantification for the ratio of phosphorylated T389 S6K1 with total S6K1 from ***G*** (one-way ANOVA; $F_{(5,\ 12)} = 52.55$; $p < 0.0001$). ***J***, Representative immunoblots from DIV 14 neuronal lysates with the same treatment conditions as described in ***D***. ***K***, Bar graph quantification for the ratio of phosphorylated S473 Akt with total Akt from ***J*** (one-way ANOVA; $F_{(5,\ 12)} = 15.41$; $p < 0.0001$). ***L***, Bar graph quantification for the ratio of phosphorylated T389 S6K1 with total S6K1 from ***J*** (one-way ANOVA; $F_{(5,\ 12)} = 14.42$; $p = 0.0001$). Quantifications are from $n = 3$ individual replicates for each treatment condition and time point using one-way ANOVA, Tukey's multiple comparisons.

Using a high-throughput multiplex TMT labeling approach, we identified 6,744 total proteins with a stringent FDR < 0.01 across the four conditions. Reelin stimulation led to significant changes within the proteome when compared with the mock control after 30 min (Fig. 2*A*). In contrast, GST-RAP treatment regulated protein expression in the opposite direction compared with the Reelin group ($p < 0.05$; Fig. 2*A*), likely due to RAP's effects on blocking Reelin binding to Apoer2 and Vldlr. Interestingly, we observed a distinct expression pattern of proteomic changes in the Reelin and GST-RAP treatment condition indicating Reelin signaling through the noncanonical pathway has a substantial and distinct impact on the proteome.

To examine how the canonical and noncanonical Reelin pathways differ functionally, we performed gene set enrichment

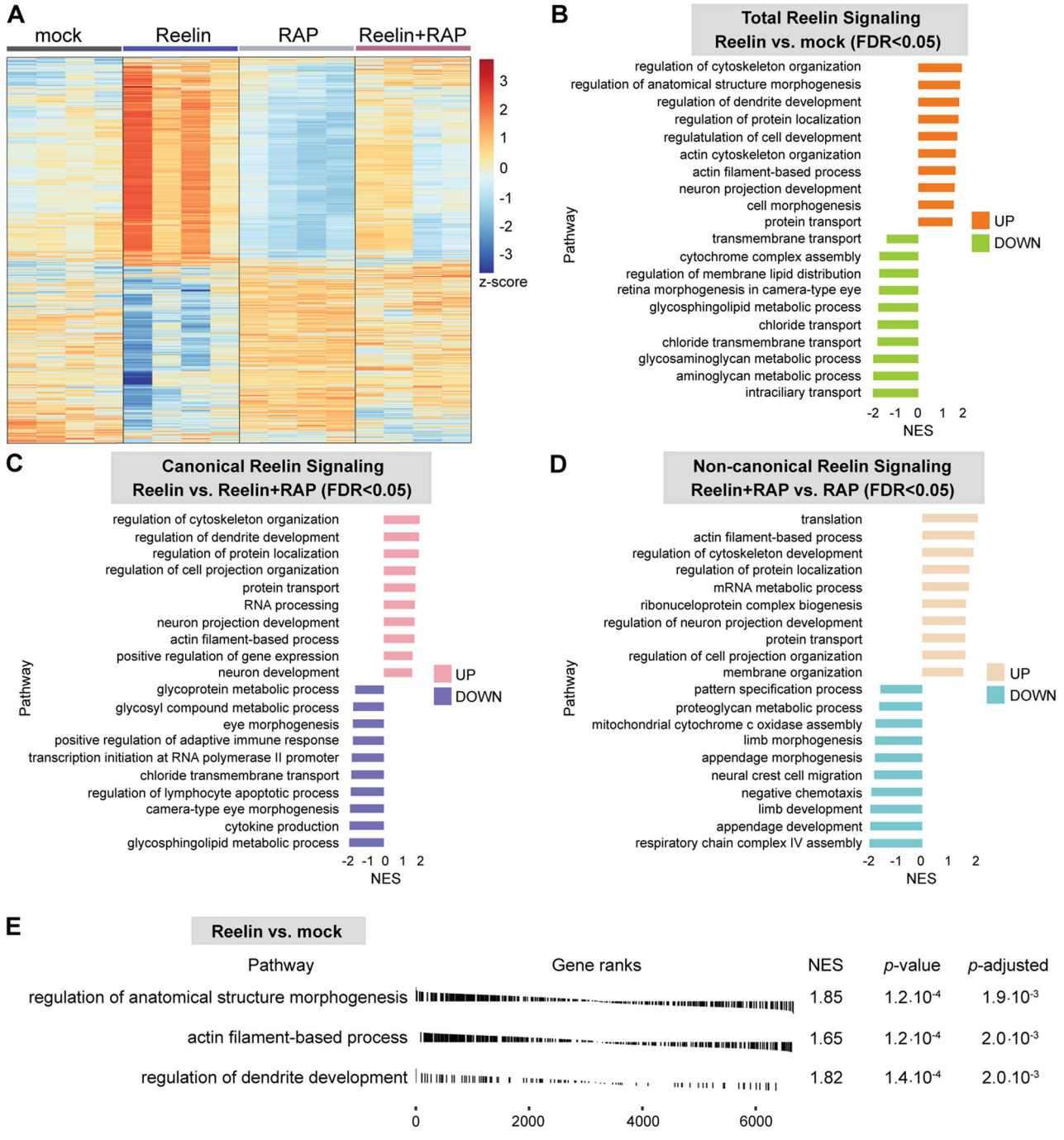

Figure 2. Proteomic analysis of acute Reelin signaling. Primary murine cortical neurons at DIV 7 were treated with the mock control, 50 nM Reelin for 30 min, 100 nM GST-RAP for 2 h, or Reelin with GST-RAP (2 h prior to 30 min Reelin stimulation) and subjected to TMT LC-MS/MS. ***A***, Heatmap of proteome clusters indicating differentially expressed proteins (rows) that are significantly upregulated (red) and downregulated (blue). ***B***, A two-side bar plot of GSEA pathways identified from the Reelin and mock control comparison with FDR < 0.05. The numbers at the bottom are NES for the corresponding biological pathway categories that are up- and downregulated of the ranked list. ***C***, Two-side bar plot of GSEA pathways identified from the Reelin and Reelin with RAP comparison with FDR < 0.05 representing the canonical Reelin pathway. ***D***, Two-side bar plot of GSEA pathways identified from the Reelin with RAP and RAP alone comparison with FDR < 0.05 representing the noncanonical Reelin pathway. ***E***, Gene ranking plot of several developmental and cytoskeletal associated pathways enriched in Reelin stimulation compared with the mock control; $p \leq 0.02$. See Extended Data Figures 2-1 and 2-2 for more details.

analysis on the TMT dataset. We ranked all genes according to the extent of their differential expression between the groups and computed NES for the collection of gene sets representing biological pathways and identified gene sets that are up- and downregulated of the ranked list. When we compared the Reelin-treated group with the mock control where the difference represents the total effect of Reelin, we found upregulated pathways related to regulation of cytoskeleton organization, anatomical structure morphogenesis, dendrite development, protein localization and transport, cell development and morphogenesis, actin cytoskeleton organization, actin filament-based process, and neuron projection development (FDR < 0.05; Fig. 2*B*). In contrast, downregulated genes belonged to gene sets associated with intraciliary transport, aminoglycan, glycosaminoglycan and glycosphingolipid metabolic process, and chloride transport (Fig. 2*B*). Interestingly, a majority of the upregulated pathways in total Reelin signaling overlapped with canonical Reelin signaling when we compared the Reelin-treated group with the Reelin- and RAP-treated group including regulation of cytoskeleton organization, dendrite development, protein localization and transport, neuron projection development, and actin filament-based process (Fig. 2*C*). This also coincided with downregulated pathways including glycosphingolipid metabolic process and chloride transmembrane transport. This was not surprising given the preferential binding of Reelin to the lipoprotein receptors Apoer2 and Vldlr. GSEA also identified gene sets unique to the canonical Reelin signaling pathway, including the upregulation of RNA processing and positive regulation of gene expression and the downregulation of cytokine production and regulation of lymphocyte apoptotic process. When we examined noncanonical Reelin signaling by comparing the Reelin and RAP-treated group with RAP alone, we identified several significantly enriched gene sets unique to the noncanonical Reelin pathway, including translation, actin filament-based process, regulation of cytoskeleton development, regulation of protein localization, mRNA metabolic process, and ribonucleoprotein complex biogenesis. We noted several downregulated pathways related to respiratory chain complex IV assembly, appendage, and limb development and morphogenesis. We also observed pathway cross talk between the canonical and noncanonical Reelin signaling pathways related to regulation of protein localization, protein transport, and actin filament-based process, whereas groups such as regulation of cytoskeleton organization and regulation of dendrite development are preferentially induced by the canonical pathway (Fig. 2*C*,*D*). Together, these data show that Reelin stimulation regulates proteomic networks associated with regulation of anatomical structure morphogenesis and dendrite development, particularly related to actin filament-based process at DIV 7 (Fig. 2*E*).

Reelin stimulation regulates actin filament dynamics in developing neurites

Because we observed an enrichment of gene sets related to regulation of cytoskeleton development and organization, including actin filament-based process following Reelin stimulation, we explored whether Reelin functionally plays a role in actin filament dynamics in developing neurons. To test this, we stimulated DIV 7 cultured hippocampal neurons with 50 nM Reelin and performed labeling for phalloidin to probe for F-actin, a key cytoskeletal component important for cell motility and growth. Reelin stimulation led to a 23% decrease of phalloidin intensity in neurites when compared with the mock control ($p < 0.0001$; Fig. 3*A*,*B*) indicating that Reelin-treated neurons may lead to F-actin remodeling in neurites. To test whether Reelin's effects are dependent on the canonical Reelin signaling pathway, we treated neurons with 100 nM GST-RAP for 2 h prior to Reelin stimulation and found that RAP does not affect phalloidin intensity. Similarly, treating neurons with PI3K inhibitor LY294002 prevented Reelin-mediated effects on phalloidin intensity indicating the Reelin-mediated changes in phalloidin intensity are through the canonical Reelin signaling that requires PI3K activation. We next systematically examined whether the decrease in phalloidin intensity following Reelin stimulation was localized to primary or secondary neurites. We observed Reelin stimulation led to a 24% decrease in phalloidin intensity in primary neurites when compared with the mock control ($p = 0.0012$; Fig. 3*C*). In addition, we observed phalloidin intensity in the Reelin-stimulated group was 26.7% lower when we compared with the Reelin- and LY294002-treated group in secondary neurites ($p = 0.0321$; Fig. 3*D*).

In contrast, we observed a 45% increase in β-actin intensity across all neurites after Reelin stimulation compared with the mock control ($p < 0.0001$; Fig. 3*E*,*F*). Likewise, we observed a 37% increase in β-actin intensity in primary neurites ($p = 0.0059$) and a 57% increase in secondary neurites ($p = 0.0367$) after Reelin stimulation compared with the mock control (Fig. 3*G*,*H*). However, β-actin intensity was not changed in the presence of GST-RAP or LY294002. Since we did not observe any changes in β-actin protein levels by immunoblotting after Reelin stimulation (Fig. 4*E*,*H*), it is likely that the increase in β-actin intensity seen by immunofluorescence after Reelin stimulation is an increase in monomeric and/or oligomeric β-actin due to F-actin remodeling and not a result of de novo translation of β-actin. To test this further, we treated DIV 7 cultured neurons with 40 μM anisomycin, a translation inhibitor, for 45 min prior to Reelin stimulation. We observed a 25% increase in β-actin intensity across all neurites after Reelin stimulation compared with the mock control ($p < 0.0001$; Fig. 3*I*,*J*). Similarly, we observed a 30% increase in β-actin intensity in primary neurites ($p < 0.0001$; Fig. 3*I*,*K*). However, when we treated neurons with both anisomycin and Reelin, we observed a similar 30% increase in β-actin intensity across all neurites compared with the mock control ($p < 0.0001$; Fig. 3*I*,*J*) and a 50% increase compared with mock control neurons treated with anisomycin ($p < 0.0001$; Fig. 3*I*–*L*). These findings demonstrate that the increase in β-actin intensity after Reelin stimulation is not due to de novo translation.

To determine whether the cytoskeleton changes we observed were specific to actin remodeling, we immunolabeled neurons against α-tubulin, one of the building blocks for microtubules. We did not observe any α-tubulin intensity changes following Reelin treatment or in the presence of GST-RAP or LY294002 (Fig. 3*M*–*P*). We also immunostained for the microtubule-associated protein, MAP2, and did not observe any MAP2 intensity changes across all four treatment conditions in all neurites observed (Fig. 3*Q*–*T*), suggesting Reelin's effect on the cytoskeleton was specific to actin remodeling at DIV 7. Together, the increase in β-actin intensity in conjunction with the decrease in phalloidin intensity demonstrates that the canonical Reelin signaling regulates unique pools of actin that serve to dynamically regulate actin remodeling in nascent neurites important for the modulation of dendritic outgrowth in neurons.

Reelin regulates n-cofilin phosphorylation at serine3 in nascent neurites

After observing that Reelin stimulation leads to a decrease in F-actin, we next asked whether the decrease is mediated through

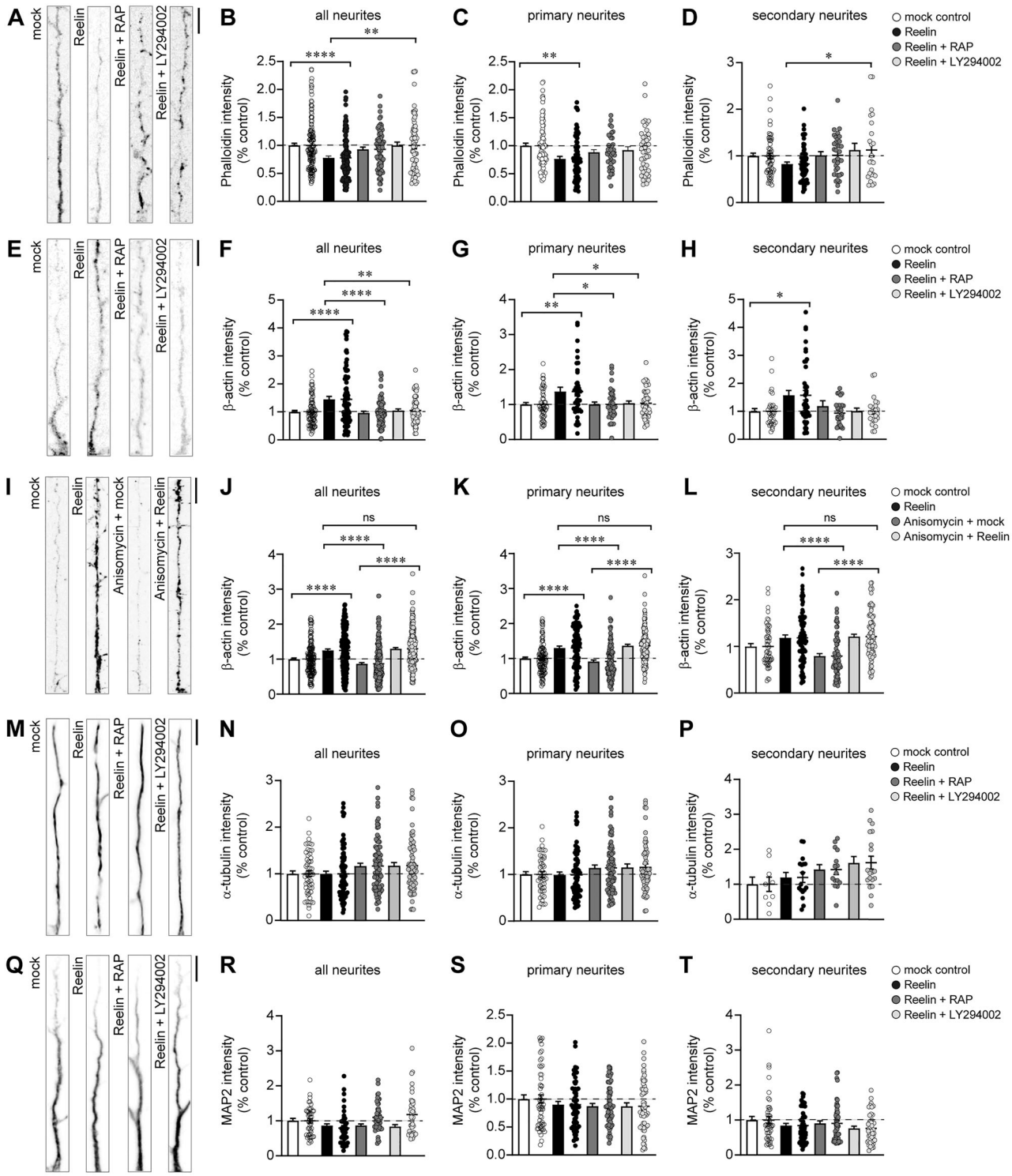

Figure 3. Reelin stimulation regulates actin remodeling in developing neurites. Primary murine hippocampal neurons at DIV 7 were treated with the mock control, 50 nM Reelin, 100 nM GST-RAP for 2 h prior to Reelin, or 50 µM LY294002 for 30 min prior to Reelin stimulation. ***A***, Representative images of neurons labeled with phalloidin showed a decrease in phalloidin intensity in neurites following Reelin stimulation. ***B***, Bar graph quantification of fluorescent phalloidin intensity in all neurites normalized to the mock control (one-way ANOVA; $F_{(3,\ 423)} = 7.879$; $p < 0.0001$). ***C***, Bar graph quantification of phalloidin intensity in primary neurites normalized to the mock control (one-way ANOVA; $F_{(3,\ 239)} = 4.820$; $p = 0.0028$). ***D***, Bar graph quantification of phalloidin intensity in secondary neurites normalized to mock control (one-way ANOVA; $F_{(3,\ 180)} = 3.307$; $p = 0.0214$). $n = 5$ independent experiments with $n = 15$–26 neurons per condition analyzed. ***E***, Representative images immunostained for β-actin showed an increase in β-actin intensity in neurites following Reelin stimulation. ***F***, Bar graph quantification of fluorescent β-actin intensity in all neurites normalized to the mock control (one-way ANOVA; $F_{(3,\ 302)} = 9.658$; $p < 0.0001$). ***G***, Bar graph quantification of β-actin intensity in primary neurites normalized to % mock control (one-way ANOVA; $F_{(3,\ 171)} = 4.695$; $p = 0.0035$). ***H***, Bar graph quantification of β-actin intensity in secondary neurites normalized to mock control (one-way ANOVA; $F_{(3,\ 127)} = 3.227$; $p = 0.0248$). $n = 3$ independent experiments with $n = 15$–16 neurons per condition analyzed. ***I***, Representative images immunostained for β-actin showed an increase in β-actin intensity in neurites following Reelin stimulation which was not affected following anisomycin treatment. ***J***, Bar graph quantification of fluorescent β-actin intensity in all neurites normalized to mock control (one-way ANOVA; $F_{(3,\ 794)} = 33.71$; $p < 0.0001$). ***K***, Bar graph quantification of β-actin intensity in primary neurites normalized to % mock control (one-way ANOVA; $F_{(3,\ 498)} = 24.45$; $p < 0.0001$). ***L***, Bar graph quantification of β-actin intensity in secondary neurites normalized to mock control (one-way ANOVA; $F_{(3,\ 292)} = 12.08$; $p < 0.0001$). $n = 2$ independent experiments with $n = 29$–30

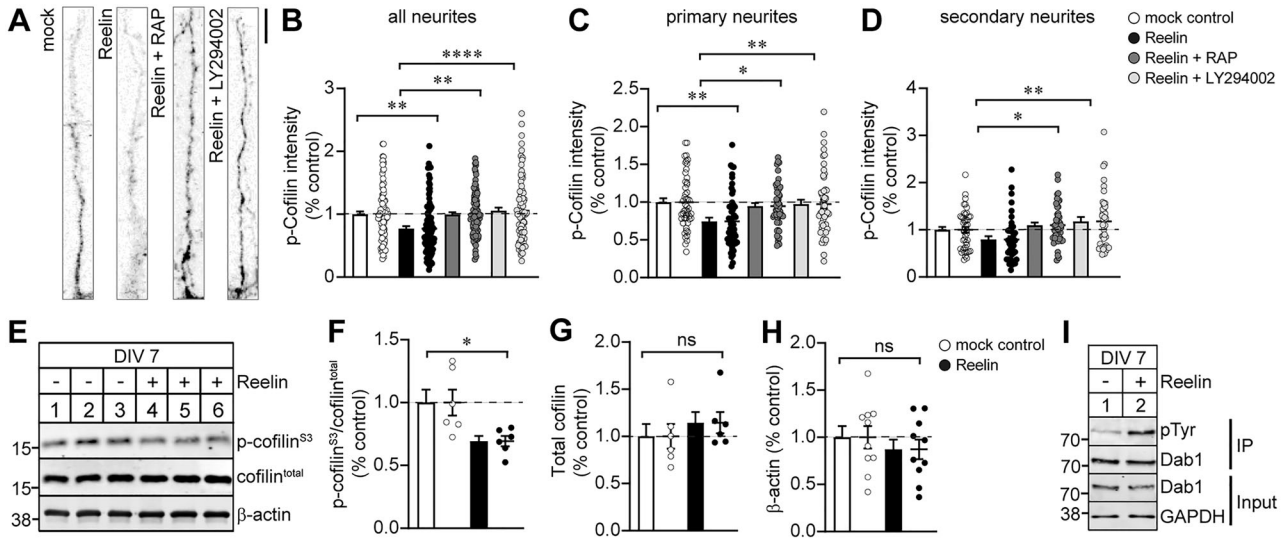

Figure 4. Reelin reduces n-cofilin phosphorylation at Ser3. ***A***, Primary murine hippocampal neurons at DIV 7 were treated with the mock control, 50 nM Reelin, 100 nM GST-RAP for 2 h prior to Reelin, or 50 µM LY294002 for 30 min prior to Reelin stimulation. Representative images immunostained for phospho-cofilin at Ser3 showed a decrease in phospho-cofilin in neurites following Reelin stimulation. Scale bar, 10 µm. ***B***, Bar graph quantification of fluorescent phospho-cofilin intensity in all neurites normalized to mock control (one-way ANOVA; $F_{(3,\ 383)} = 8.602$; $p < 0.0001$). ***C***, Bar graph quantification of phospho-cofilin intensity in primary neurites normalized to % mock control (one-way ANOVA; $F_{(3,\ 203)} = 5.540$; $p = 0.0011$). ***D***, Bar graph quantification of phospho-cofilin intensity in secondary neurites normalized to mock control (one-way ANOVA; $F_{(3,\ 176)} = 5.500$; $p = 0.0012$). $n = 3$ independent experiments with $n = 14$–16 neurons per condition analyzed using one-way ANOVA, Tukey's multiple comparisons. ***E***, Representative immunoblots from DIV 7 neuronal cortical lysates treated with 50 nM Reelin or mock control for phospho-cofilin at Ser3, total n-cofilin, and β-actin. ***F***, Bar graph quantification for the ratio of phosphorylated cofilin at Ser3 with total cofilin from ***E*** shows a decrease in cofilin phosphorylation following Reelin stimulation (unpaired *t* test; $t = 2.763$; df = 10; $p = 0.0200$). ***G***, ***H***, Bar graph quantification for total cofilin and β-actin, respectively (unpaired *t* test; $t = 0.8344$; df = 10; $p = 0.4236$; $t = 0.8118$; df = 18; $p = 0.4275$). $n = 6$–10 individual replicates. ***I***, Representative immunoblots showing phosphotyrosine levels after Dab1 IP from primary murine cortical neurons treated with 50 nM Reelin or mock control for 30 min at DIV 7. Total Dab1 and GAPDH serve as loading controls (input). ns, not significant.

the actin severing protein, n-cofilin, since it has been reported that Reelin signaling modulates serine3 phosphorylation of n-cofilin (Chai et al., 2009; Leemhuis et al., 2010). A decrease in phosphorylation at serine3 promotes n-cofilin to sever F-actin which allows for actin rearrangement in cell motility and navigation (Agnew et al., 1995; Carlier et al., 1997; Ghosh et al., 2004; Bravo-Cordero et al., 2013; Q. Chen et al., 2015). To test this, we immunolabeled against phospho-cofilin at serine3 in primary murine hippocampal neurons following Reelin stimulation for 30 min. We found that Reelin decreased phospho-serine3-cofilin intensity by 23% when compared with the mock control ($p = 0.0011$; Fig. 4*A*,*B*). The effect of phospho-serine3-cofilin intensity after Reelin stimulation was abolished in neurons treated with GST-RAP and LY294002, indicating that Reelin's effects on n-cofilin phosphorylation are dependent on the canonical Reelin pathway. In addition, we found a similar 25% decrease in phospho-serine3-cofilin intensity in primary neurites after Reelin stimulation compared with the mock control ($p = 0.0021$; Fig. 4*C*). While not significant, we observed a 21% decrease in phospho-serine3-cofilin intensity between Reelin and mock in secondary neurites ($p = 0.1692$; Fig. 4*D*). We did, however, observe a significant 27.5 and 32.5% decrease in phospho-serine3-cofilin intensity when we compared the Reelin-treated group with neurons treated with GST-RAP ($p = 0.0104$) and LY294002 ($p = 0.0012$) in secondary neurites, respectively (Fig. 4*D*).

We also compared the levels of phosphorylated n-cofilin protein from neuronal lysates collected from DIV 7 primary cortical neurons stimulated with Reelin by immunoblotting for both serine3 phosphorylation of n-cofilin and total n-cofilin. Western blot analysis showed that Reelin significantly decreased the ratio of phosphorylated n-cofilin at serine3 to total cofilin by 31% ($p = 0.02$; Fig. 4*E*,*F*, Lanes 4–6). However, we did not observe any effect of Reelin on total cofilin or β-actin protein levels (Fig. 4*G*,*H*). To confirm that Reelin was effectively stimulating the Dab1 signaling pathway in primary cortical neurons, we performed Dab1 IP to monitor Dab1 phosphorylation activity by immunoblotting with an anti-phosphotyrosine antibody and demonstrated Reelin consistently increased the levels of phosphorylated Dab1 in immunoprecipitates (Fig. 4*I*, Lane 2) compared with mock medium (Lane 1) at DIV 7. Taken together, our data suggest acute Reelin signaling through the canonical Reelin–PI3K pathway regulates n-cofilin phosphorylation at serine3 in nascent neurites in culture.

←

neurons per condition analyzed. ***M***, Representative images immunostained for alpha-tubulin (α-tubulin). ***N***, Bar graph quantification of fluorescent α-tubulin intensity in all neurites normalized to mock control (one-way ANOVA; $F_{(3,\ 299)} = 2.514$; $p = 0.0585$). ***O***, Bar graph quantification of α-tubulin intensity in primary neurites normalized to mock control (one-way ANOVA; $F_{(3,\ 239)} = 1.780$; $p = 0.1517$). ***P***, Bar graph quantification of α-tubulin intensity in secondary neurites normalized to mock control (one-way ANOVA; $F_{(3,\ 56)} = 2.239$; $p = 0.0938$). $n = 2$ independent experiments with $n = 26$–28 neurons per condition analyzed. ***Q***, Representative images immunostained for MAP2. ***R***, Bar graph quantification of fluorescent MAP2 intensity in all neurites normalized to mock control (one-way ANOVA; $F_{(3,\ 414)} = 1.950$; $p = 0.1208$). ***S***, Bar graph quantification of MAP2 intensity in primary neurites normalized to mock control (one-way ANOVA; $F_{(3,\ 220)} = 1.010$; $p = 0.3891$). ***T***, Bar graph quantification of MAP2 intensity in secondary neurites normalized to mock control (one-way ANOVA; $F_{(3,\ 191)} = 1.652$; $p = 0.1788$). $n = 3$ independent experiments with $n = 16$–18 neurons per condition analyzed. All analysis was examined using one-way ANOVA, Tukey's multiple comparisons. Scale bars, 10 µm. ns, not significant.

Reelin stimulation leads to de novo translation of aldolase A and mobilizes aldolase A from the cytoskeleton

Based on the total Reelin GSEA dataset in Figure 2, *B* and *E*, that showed Reelin stimulation regulates proteomic networks associated with regulation of anatomical structure morphogenesis and dendrite development, particularly related to actin filament-based process at DIV 7, we identified aldolase A, a glycolytic enzyme and actin-binding protein, from the quantitative proteomic dataset as a novel effector of the total Reelin signaling pathway that may contribute to actin remodeling changes. Aldolase A was within the regulation of anatomical structure and cell morphogenesis pathway identified by GSEA. Several pieces of evidence support that aldolase A may play a role in Reelin-mediated neurite growth. First, aldolase A is a well known F-actin–binding protein shown to regulate cell motility in non-neuronal cells (Tochio et al., 2010; Ritterson Lew and Tolan, 2013). Second, aldolase A is expressed in the brain during early developmental time points that are associated with cell migration, growth, and extensive cytoskeletal reorganization (Weber, 1965; Lebherz and Rutter, 1969; Penhoet et al., 1969). Third, previous studies have shown that aldolase A and n-cofilin compete for the same binding site on F-actin (Gizak et al., 2019) and the inhibition of the aldolase A and actin interaction leads to loss of F-actin stress fibers in a n-cofilin–dependent manner (Gizak et al., 2019; Sun et al., 2021). Lastly, aldolase A is an effector of the insulin-PI3K pathway that regulates epithelial cell's metabolism through mobilization of aldolase A from the actin cytoskeleton (Hu et al., 2016). Given that we showed Reelin regulates actin dynamics and n-cofilin phosphorylation through PI3K signaling pathway, we posit that aldolase A may serve as a molecular effector of Reelin-mediated dendrite growth.

To confirm whether Reelin leads to changes in aldolase A protein level expression, neuronal lysates collected from DIV 7 primary cortical neurons stimulated with 50 nM Reelin or mock for 30 min were immunoblotted for aldolase A and β-actin. Western blot analysis showed that Reelin caused a 22% increase in aldolase A levels when compared with the mock control ($p = 0.0342$; Fig. 5*A*,*B*). The effect of aldolase A after Reelin stimulation was prevented in neurons treated with GST-RAP or LY294002 indicating the increase in aldolase A protein levels was mediated through the canonical Reelin–PI3K signaling pathway. To determine whether the increase in aldolase A protein levels was a result of de novo translation or reduced protein degradation, we treated DIV 7 neurons with 40 μM anisomycin, a translation inhibitor, for 45 min prior to Reelin stimulation. Western blot analysis showed that Reelin caused a 46.5% increase in aldolase A levels when compared with the mock control ($p = 0.0499$; Fig. 5*C*,*D*); however, this was abolished with anisomycin treatment demonstrating that the increase in aldolase A expression after Reelin stimulation may be a result of de novo translation. To rule out the possibility that the increase in aldolase A levels is due to reduced protein degradation, we treated DIV 7 cultured neurons with 50 μM MG132, a proteasome inhibitor, for 4 h prior to Reelin stimulation. We did not detect any changes in aldolase A levels in Reelin-stimulated neurons treated with MG132 ($p = 0.347$; Fig. 5*E*). This suggests that inhibition of the proteasome degradation pathway did not affect Reelin-induced aldolase A expression levels and the increase is likely due to de novo translation. It is important to note that quantitative proteomics is typically based on the measurement of multiple spectra and peptides per protein that is accompanied by statistical confidence measures for each peptide; thus, it has higher sensitivity of detecting protein changes compared with Western blotting approaches.

Previous studies had shown that aldolase A is mobilized from the actin cytoskeleton through PI3K activation in epithelial cells (Hu et al., 2016). To determine whether aldolase A is mobilized from the actin cytoskeleton through Reelin-PI3K signaling in primary murine cortical neurons, we performed a digitonin permeabilization assay to allow for efflux of diffusible aldolase A and estimate the fraction of aldolase A in the soluble versus immobilized state based on separate collection of supernatant and cell lysates, respectively. DIV 7 neurons were treated with either mock, Reelin, RAP, or LY294002 prior to Reelin stimulation and subsequently permeabilized with digitonin for 5 min at 4°C. We found a 35% increase in aldolase A in the supernatant fraction induced by Reelin stimulation indicating an increase in mobilized aldolase A when compared with the mock control ($p = 0.0337$; Fig. 5*F*,*G*, Lanes 3–4). Both RAP and LY294002 prevented the Reelin-mediated effect on aldolase A mobilization. In fact, LY294002 reduced aldolase A mobilization by 39% compared with the mock control ($p = 0.0111$; Fig. 5*F*,*G*, Lanes 7–8). We did not detect any aldolase A in the supernatant from neurons that were not permeabilized with digitonin which served as a negative control for the assay (Fig. 5*F*, Lanes 9–12). In summary, these results indicate that the effects of Reelin on aldolase A levels and mobilization from the cytoskeleton are dependent on the activation of PI3K.

Aldolase A functions downstream of Reelin signaling in regulating dendrite growth

To directly test whether aldolase A functions downstream of Reelin signaling, we infected primary murine hippocampal neurons with lentiviral *Aldoa* shRNA targeting sequences in the 3′-UTR region at DIV 1. We found that *Aldoa* shRNA efficiently downregulated aldolase A protein expression at DIV 7 and resulted in a significant 64% knockdown compared with *scrambled* (*scr*) control shRNA ($p = 0.0179$; Fig. 6*A*,*B*, Lane 2). In contrast, infection of lentiviral *Aldoa* shRNA in neurons had no effect on β-actin levels (Fig. 6*A*,*B*). Since aldolase A is one of the two aldolase isozymes that is expressed in the brain, we also immunoblotted for aldolase C and found no difference in aldolase C levels demonstrating that *Aldoa* shRNA is specific to aldolase A (Fig. 6*A*,*B*).

To investigate whether aldolase A functions downstream of Reelin signaling on dendritic branching, primary murine hippocampal neurons were infected at DIV 1 with *scr* or *Aldoa* shRNA, and starting at DIV 4, neurons were treated with 50 nM Reelin or the mock control once a day for 72 h and immunolabeled against dendritic marker, MAP2 at DIV 7. We performed Sholl analysis to examine global changes in neuronal morphology, specifically the complexity of the dendritic arbor and the overall pattern of arborization. Sholl analysis revealed that shRNA knockdown of aldolase A greatly reduced dendritic growth where it shifted the distribution downward and to the left compared with *scr* shRNA neurons, indicating both a decrease in the number and length of the neurites (Fig. 6*C*,*D*). The average total neurite length was 49.5% shorter in neurons infected with *Aldoa* shRNA compared with *scr* shRNA-infected neurons ($p < 0.0001$; Fig. 6*E*). Similarly, the average maximum neurite length was decreased by 40% in *Aldoa* shRNA-infected neurons ($p < 0.0001$; Fig. 6*F*) but had no effect on the average minimum neurite length between *scr* and *Aldoa* shRNA-infected neurons (Fig. 6*G*). Meanwhile, Reelin induced a 32% increase in the average total neurite length in *scr* shRNA neurons compared with the mock control ($p < 0.0001$; Fig. 6*E*). Similarly, the average maximum length of the longest neurite was increased by 31% following Reelin stimulation ($p = 0.0002$; Fig. 6*F*) but had no effect in the average minimum neurite length (Fig. 6*G*). Interestingly, Reelin stimulation

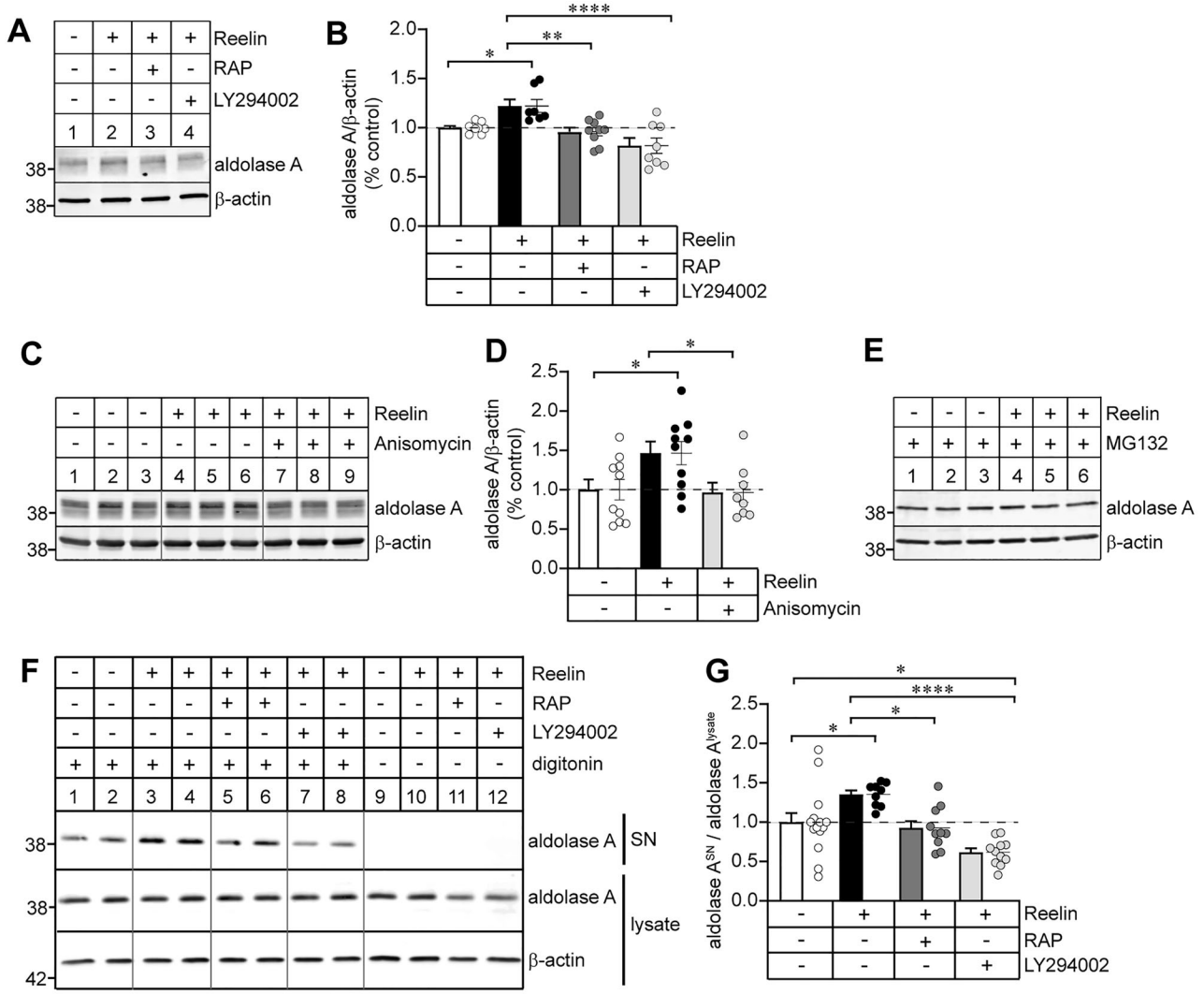

Figure 5. Aldolase A undergoes de novo translation and mobilizes from the cytoskeleton in response to Reelin stimulation. ***A***, Representative immunoblots of DIV 7 neuronal cortical lysates treated with the mock control, 50 nM Reelin, 100 nM GST-RAP for 2 h prior to Reelin, or 50 μM LY294002 for 30 min prior to Reelin stimulation for aldolase A and β-actin. ***B***, Bar graph quantification of aldolase A normalized to mock control showed an increase in aldolase A protein levels after Reelin stimulation (one-way ANOVA; $F_{(3, 29)} = 8.998$; $p = 0.0002$). $n = 7–9$ individual replicates. ***C***, Representative immunoblots of DIV 7 neuronal lysates treated with mock control (Lanes 1–3), 50 nM Reelin (Lanes 4–6), or 40 μM anisomycin for 45 min prior to Reelin stimulation (Lanes 7–9) for aldolase A and β-actin. ***D***, Bar graph quantification of aldolase A normalized to mock control showed an increase in aldolase A protein levels after Reelin stimulation but not in anisomycin-treated neurons (one-way ANOVA; $F_{(2, 25)} = 4.275$; $p = 0.0253$). $n = 8–10$ individual replicates. ***E***, Representative immunoblots of DIV 7 neuronal lysates collected from neurons that were treated with 50 μM MG132 for 4 h prior to mock (Lanes 1–3) or Reelin stimulation (Lanes 4–6) and subjected to immunoblotting for aldolase A and β-actin. $n = 3$ individual replicates. ***F***, Representative immunoblots of DIV 7 neuronal lysates treated with the mock control, 50 nM Reelin, 100 nM GST-RAP for 2 h prior to Reelin, or 50 μM LY294002 for 30 min prior to Reelin stimulation and subjected to digitonin permeabilization (Lanes 1–8). Supernatant (SN) and cell lysate were subjected to immunoblotting for aldolase A and β-actin as indicated. ***G***, Quantification of aldolase A in the diffusible fraction (supernatant) to immobile (cell lysate) fraction show an increase in aldolase A in response to Reelin stimulation (one-way ANOVA; $F_{(3, 41)} = 10.45$; $p < 0.0001$). $n = 9–15$ individual replicates using one-way ANOVA, Tukey's multiple comparisons.

had no effect in neurons following aldolase A knockdown compared with *Aldoa* shRNA-infected neurons alone ($p = 0.3870$ neurite sum length, $p = 0.8237$ maximum neurite length, and $p = 0.9864$ minimum neurite length; Fig. 6*E–G*). To exclude any potential off-target effects, we also examined at least two other *Aldoa* shRNAs (targeting different sequences within the ORF of *Aldoa*) and found a similar phenotype (Extended Data Fig. 6-1) further confirming that aldolase A is downstream of Reelin signaling and is essential for Reelin-induced dendritic outgrowth.

Aldolase A knockdown disrupts neuronal morphology in vivo

Since we found aldolase A functions downstream of the Reelin signaling pathway, we next asked whether aldolase A knockdown impacts neuronal migration and architecture in vivo. To test this, we performed IUE with GFP-tagged *scr* or *Aldoa* shRNA on mouse embryos at E15.5 and analyzed both the position of GFP-positive cells within the cortical layers and morphology located in the primary somatosensory cortex at P14 to account for uniform distribution of cells along the rostrocaudal axis. As expected, we found most GFP-positive neurons electroporated with *scr* shRNA were in upper Layers 2 and 3 that expressed Satb2 which we used as a marker to distinguish cortical layers for analysis (Fig. 7*A*,*B*). Interestingly, we found neurons electroporated with *Aldoa* shRNA distributed deeper within Layers 2 and 3. We, therefore, measured the distance of the soma from the pia and compared neurons electroporated with *scr* and *Aldoa* shRNA. We found neurons electroporated with *Aldoa* shRNA were 57.75 μm deeper in the cortex compared with *scr*

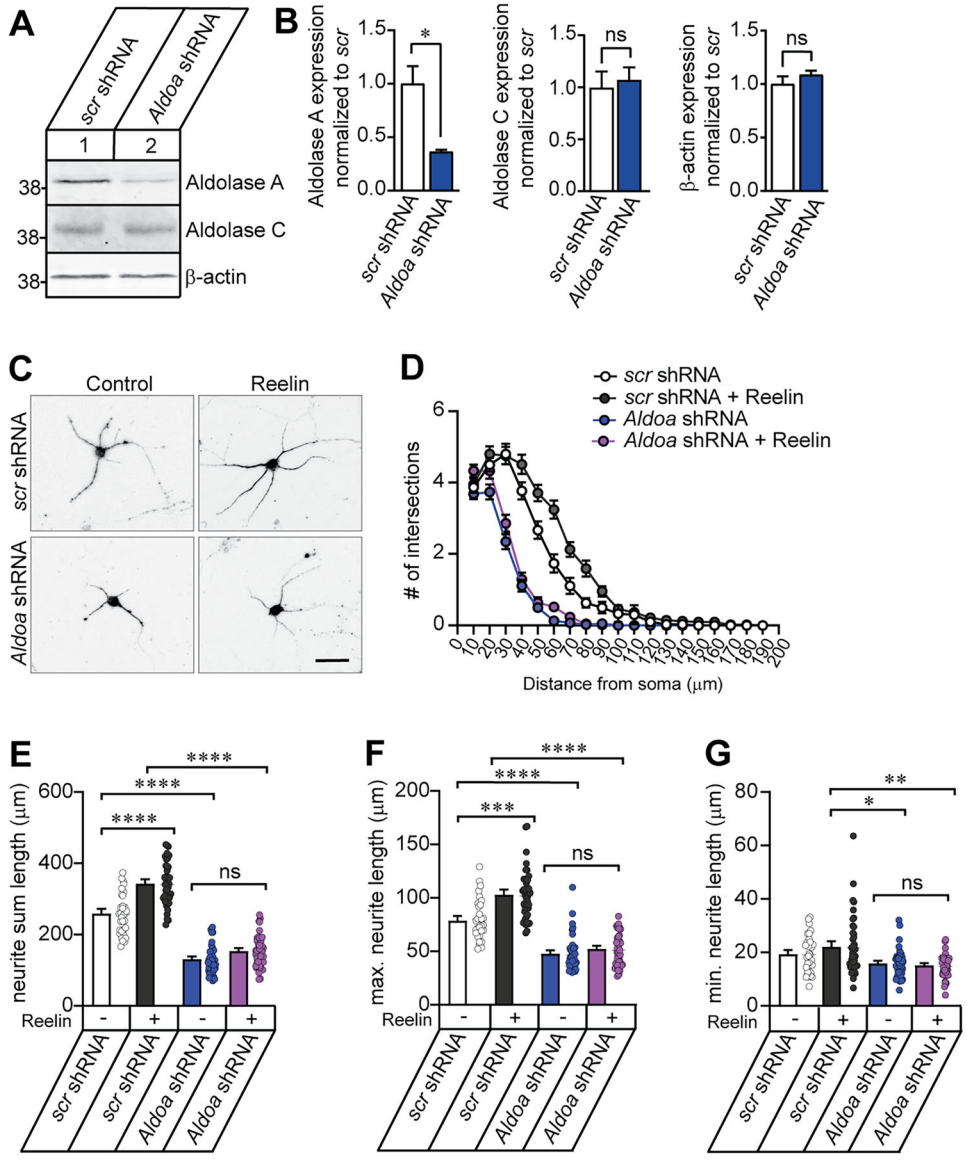

Figure 6. Aldolase A is necessary for Reelin-mediated neurite outgrowth and arborization. Primary murine hippocampal neurons on DIV 1 were infected with *scr* or *Aldoa* shRNA and analyzed at DIV 7. ***A***, Representative immunoblots showing aldolase A and aldolase C levels from DIV 7 neuronal lysate after infection with *scr* or *Aldoa* shRNA. β-actin served as loading control. ***B***, Bar graph quantifications of aldolase A, aldolase C, and β-actin expression normalized to *scr* shRNA showed a decreased protein level specifically for aldolase A (unpaired *t* test; $t = 3.874$; $df = 4$; $p = 0.0179$), but not for aldolase C (unpaired *t* test; $t = 0.3822$; $df = 6$; $p = 0.7155$) or β-actin (unpaired *t* test; $t = 1.068$; $df = 6$; $p = 0.3267$). $n = 3$ individual replicates. ***C***, Representative images of DIV 7 neurons infected with *scr* or *Aldoa* shRNA and stimulated with either the mock control or 50 nM Reelin once a day for 72 h starting at DIV 4 and immunostained against MAP2 at DIV 7. Scale bar, 12.5 μm. ***D***, Sholl analysis comparing neuronal arborization complexity between *scr* and *Aldoa* shRNA with mock and Reelin treatment showed reduced dendritic growth, and arborization in aldolase A knockdown neurons and Reelin stimulation had no effect in neurons following aldolase A knockdown (two-way ANOVA; $F_{(54, 2,793)} = 21.80$; $p < 0.0001$). $n = 3$ independent experiments with $n = 30$–42 cells per condition analyzed. ***E***, Bar graph quantification of the average total neurite sum length (one-way ANOVA; $F_{(3, 157)} = 89.41$; $p < 0.0001$). ***F***, Bar graph quantification of the average maximum neurite sum length (one-way ANOVA; $F_{(3, 158)} = 46.06$; $p < 0.0001$). ***G***, Bar graph quantification of the average minimum neurite length (one-way ANOVA; $F_{(3, 158)} = 5.149$; $p = 0.0020$). For ***E–G***, $n = 3$ independent experiments with $n = 32$–44 cells per condition analyzed using one-way ANOVA, Tukey's multiple comparisons. ns, not significant. See Extended Data Figure 6-1 for more details.

electroporated neurons ($p < 0.0001$; Fig. 7*C*). We investigated further by examining the lamina distribution of lower- and upper-level cortical neurons by immunostaining for Brn2, a marker for Layers 2/3 and 5. We found that *Aldoa* knockdown neurons colocalized with Brn2 similar to *scr* shRNA electroporated neurons suggesting that aldolase A knockdown did not affect the neuronal lamina distribution of upper-level cortical neurons (Extended Data Fig. 7-1).

We next examined whether aldolase A is necessary for proper neuronal growth and arborization and performed Sholl analysis on neurons electroporated with *scr* or *Aldoa* shRNA. Sholl analysis revealed aldolase A knockdown neurons exhibited a significant reduction in both dendritic length and arbor complexity compared with *scr* electroporated neurons ($p < 0.0001$; Fig. 7*D*,*E*). The average total neurite length was 65.6% shorter in aldolase A knockdown neurons compared with *scr* electroporated neurons ($p < 0.0001$; Fig. 7*F*). Similarly, the average maximum neurite length was decreased by 53.4% in *Aldoa* shRNA electroporated neurons ($p < 0.0001$; Fig. 7*G*). Interestingly, we found a small and significant increase in the average minimum neurite length between *scr* and *Aldoa* shRNA electroporated neurons ($p = 0.0133$; Fig. 7*H*).

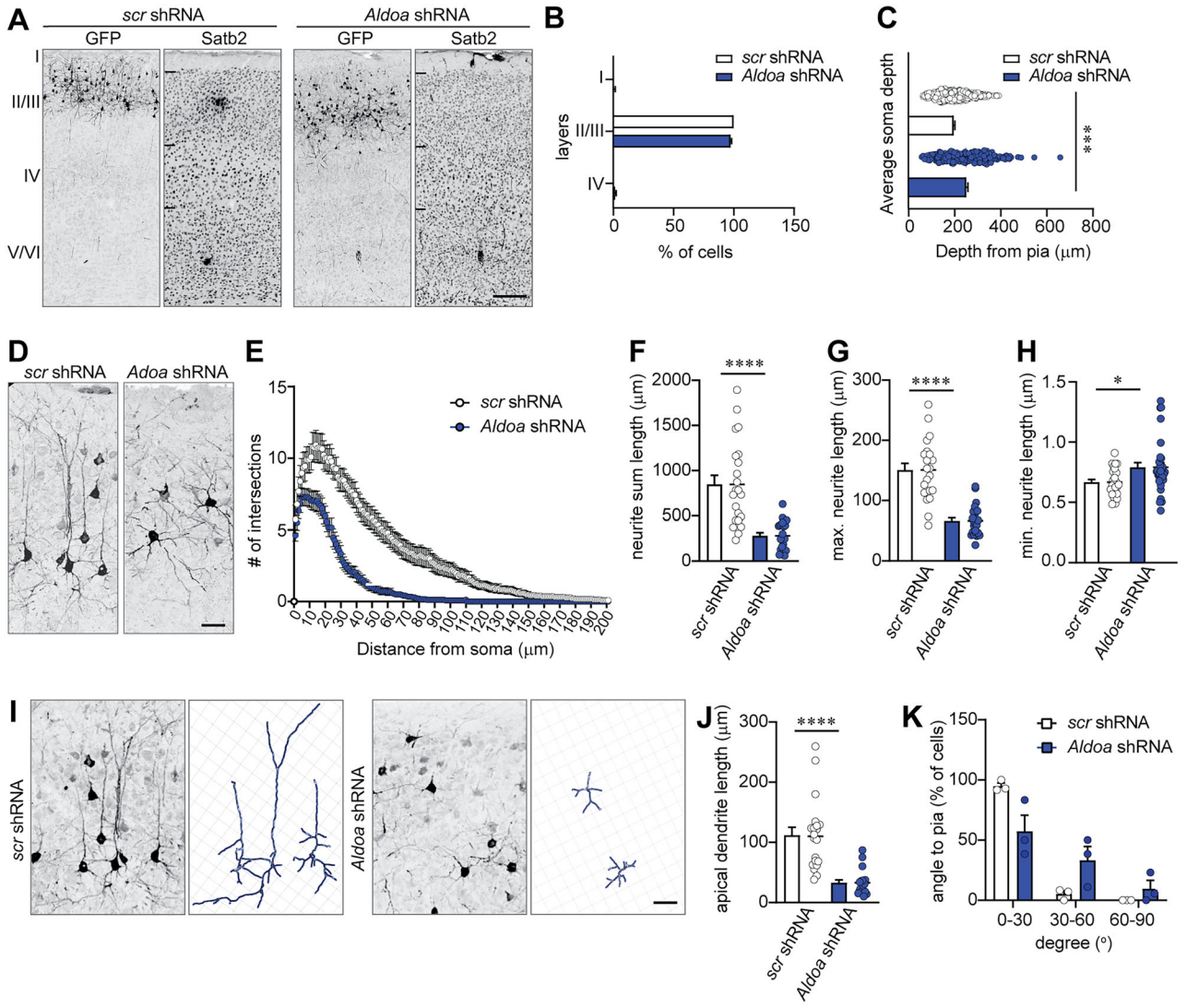

Figure 7. Aldolase A is required for neuronal arborization and apical dendrite polarity in the mouse cortex. Mouse embryos were electroporated in utero with GFP-tagged *scr* control or *Aldoa* shRNA at E15.5 and analyzed at P14. ***A***, Representative images of brain sections electroporated with GFP-tagged *scr* control or *Aldoa* shRNA and immunostained against GFP and Satb2 to visualize electroporated cells and marker to distinguish cortical layers in the somatosensory S1 cortex, respectively. Scale bar, 175 µm. ***B***, Bar graph quantification showing the percentage of GFP-positive neurons across cortical layers between *scr* and *Aldoa* shRNA electroporated neurons (two-way ANOVA; $F_{(2,\ 12)} = 7.070$; $p = 0.0094$). $n = 3$ mice per group with $n = 402–639$ cells per group analyzed. ***C***, Bar graph quantification showing the average soma depth of GFP-positive electroporated neurons from the pia showed aldolase A knockdown neurons reside deeper in the cortex compared with *scr* electroporated neurons (unpaired *t* test; $t = 7.889$; df = 556; $p < 0.0001$). $n = 3$ brains per group with $n = 264–294$ cells per group analyzed. ***D***, Representative images of GFP-positive neurons in Layers 2/3 of S1 from brains electroporated at E15.5 with *scr* or *Aldoa* shRNA showing the disrupted morphology and arborization of aldolase A knockdown neurons compared with *scr* control. Scale bar, 25 µm. ***E***, Sholl analysis showed aldolase A knockdown neurons have shorter total neurite length and less neuronal arborization compared with *scr* control neurons. A two-way ANOVA was used to determine the statistical significance of the interaction between the length of the neurites and number of crossings at each radius for each treatment condition (two-way ANOVA; $F_{(222,\ 14{,}718)} = 14.06$; $p < 0.0001$). $n = 3$ brains per condition and $n = 31–37$ neurons per condition analyzed. ***F***, Bar graph quantification showing aldolase A knockdown neurons led to a decrease in the average neurite sum length compared with *scr* control electroporated neurons (unpaired *t* test; $t = 6.478$; df = 63; $p < 0.0001$). ***G***, Bar graph quantification of the average maximum neurite length between *scr* and *Aldoa* shRNA electroporated neurons (unpaired *t* test; $t = 7.272$; df = 62; $p < 0.0001$). ***H***, Bar graph quantification of the average minimum neurite length between *scr* and *Aldoa* shRNA electroporated neurons (unpaired *t* test; $t = 2.559$; df = 55; $p = 0.0133$). For ***F–H***, $n = 3$ brains per group with $n = 25–35$ neurons analyzed. ***I***, Representative images of GFP-positive neurons in Layers II/III of S1 from brains electroporated with either *scr* or *Aldoa* shRNA (left panel) and IMARIS generated 3D wire structure reconstruction of the same neurons (right panel) showing their morphology and apical neurite orientation and length is altered in aldolase A knockdown neurons. Scale bar, 25 µm. ***J***, Bar graph quantification showing a reduction in the average length of apical neurites for aldolase A knockdown neurons (unpaired *t* test; $t = 6.164$; df = 65; $p < 0.0001$). $n = 3$ brains per group and $n = 33–34$ neurons analyzed. ***K***, The percentage of GFP-positive neurons with an apical dendrite oriented between 0–30, 31–60, and 61–90° to the pia were quantified. Quantification revealed control electroporated neurons have apical dendrites oriented mostly within 0–30° compared with aldolase A knockdown neurons (two-way ANOVA; $F_{(2,\ 12)} = 9.129$; $p = 0.0039$). $n = 3$ brains per group with $n = 30–35$ neurons analyzed using two-way ANOVA, Šídák's multiple comparisons. See Extended Data Figure 7-1 for more details.

Not only did aldolase A knockdown neurons have a significant decrease in neurite length and arborization, it was apparent they also lacked the apical–basal polarity typical of cortical pyramidal neurons (Fig. 7*I*). As such, we measured the length and orientation of the apical dendrite in GFP-positive neurons of *scr* control and *Aldoa* shRNA electroporated neurons at P14. Our results demonstrate that aldolase A knockdown caused a 69.24% decrease in the length of the apical dendrite when compared with controls ($p < 0.0001$; Fig. 7*J*). We examined apical dendrite orientation and calculated this as an angle in relation to the pial surface and binned the data into three groups: 0–30, 31–60, and 61–90° from the pial surface. Nearly 94.83% of

GFP-positive neurons electroporated with *scr* control had their apical dendrite oriented between 0 and 30° to the pia. However, only 57.26% of aldolase A knockdown neurons kept this normal, apical orientation ($p = 0.017$; Fig. 7*K*). Instead, we found nearly 33.2% of aldolase A knockdown neurons had an apical dendrite oriented between 31 and 60° and 9.55% had their apical dendrite between 61 and 90°, both trending higher when compared with *scr* control neurons. Altogether, these data support the conclusion that aldolase A is necessary for proper neuron arborization and is particularly important for the growth and orientation of the apical dendrite of pyramidal neurons in the mouse cortex.

Aldolase A requires actin-binding activity for proper neuronal arborization

Because aldolase A serves as both a glycolytic enzyme and actin-binding protein, it is in a unique position to regulate the metabolic demands and the structural rearrangements of the cytoskeleton necessary for the energy-intensive process of neurite growth and arborization. To determine which functional activity of aldolase A is required for proper neuronal arborization, we examined two aldolase mouse variants defective in either glycolytic (D33S) or actin-binding activity (R42A) that have been previously characterized in non-neuronal cells (Wang et al., 1996; Ritterson Lew and Tolan, 2012, 2013; Hu et al., 2016). The D33S aldolase A variant is catalytically dead but retains F-actin–binding activity, whereas the R42A variant abolishes the F-actin–binding activity but retains glycolytic activity. We generated three lentiviral mouse aldolase A constructs, WT, D33S, and R42A, and we titered each lentivirus uniformly to perform rescue experiments of aldolase A's knockdown effects on dendritic arborization. Primary murine hippocampal neurons were infected on DIV 1, and we performed immunolabeling against MAP2 at DIV 7. We compared the effects of *scr* shRNA, *Aldoa* shRNA (targeting 3′-UTR), *Aldoa* shRNA rescued with mouse aldolase A WT, catalytically dead D33S, or actin-binding–deficient R42A variant. The *Aldoa* shRNA-mediated knockdown of aldolase A decreased neurite arborization compared with *scr* shRNA ($p < 0.0001$; Fig. 8*A*,*B*). Both aldolase A WT and catalytically dead D33S rescued the *Aldoa* shRNA phenotype, whereas the actin-binding–deficient R42A was unable to rescue the neurite arborization effects of aldolase A knockdown on dendritic outgrowth (Fig. 8*A*,*B*).

We systematically measured the average total, maximum, and minimum neurite length between the conditions. The average total neurite length was 57.4% shorter in neurons infected with *Aldoa* shRNA compared with *scr*-infected neurons ($p < 0.0001$; Fig. 8*C*). Lentiviral infection with aldolase A WT and catalytically dead D33S variant fully rescued the effects of aldolase A knockdown phenotype ($p < 0.0001$; Fig. 8*C*). In contrast, the actin-binding–deficient R42A variant led to a 47.8% reduction in average total neurite length compared with *scr* shRNA and was unable to rescue the aldolase A knockdown phenotype ($p < 0.0001$; Fig. 8*C*). Similarly, the average maximum neurite length was decreased by 44.9% in *Aldoa* shRNA-infected neurons ($p < 0.0001$; Fig. 8*D*). Both aldolase A WT and D33S fully rescued the *Aldoa* shRNA phenotype ($p < 0.0001$; Fig. 8*D*); however, the R42A variant was unable to rescue the maximum neurite length following aldolase A knockdown when compared with *scr* shRNA control ($p = 0.0002$; Fig. 8*D*). Likewise, the average minimum length of the shortest neurite was rescued by the catalytically dead D33S aldolase A variant ($p = 0.0152$; Fig. 8*E*). Together, these results provide strong evidence that the actin-binding function of aldolase A is a key regulator controlling dendritic outgrowth.

Discussion

In this study, we showed Reelin selectively activates S6K1 phosphorylation through the PI3K/Akt and mTORC1 complex pathways during initial stages of axonal and dendritic outgrowth, a process that differs in mature cortical neurons in culture (Fig. 1). This aligns with previous studies that demonstrated Reelin signaling to PI3K/Akt is necessary for Reelin-induced neurite outgrowth (Beffert et al., 2002; Jossin and Goffinet, 2007; Leemhuis et al., 2010). Through an unbiased proteomics analysis to delineate between canonical and noncanonical Reelin signaling during dendritic outgrowth in primary murine cortical neurons, we found significant cross talk related to cytoskeleton regulation, neuron projection development, and actin filament-based processes (Fig. 2). Notably, gene sets influenced by the noncanonical Reelin pathway include protein translation, mRNA metabolic processes, and ribonucleoprotein complex biogenesis, highlighting distinct impacts on neuronal structure and function.

We explored how Reelin specifically influences actin and not α-tubulin dynamics in dendritic development at DIV 7 (Fig. 3). We showed that Reelin stimulation reduces F-actin intensity while increasing total β-actin intensity in developing neurites. The increase in β-actin was not corroborated by Western blot analysis, suggesting the changes we observed in immunocytochemistry might be due to an increase in monomeric actin following F-actin depolymerization and not due to de novo translation. Indeed, neurons treated with anisomycin, a translation inhibitor, had no effect on Reelin-induced β-actin intensity. Accompanying these changes was a reduction in cofilin serine3 phosphorylation (Fig. 4), indicating enhanced cofilin severing activity. This suggests that Reelin promotes cofilin-mediated actin depolymerization and rearrangement in neurites in vitro, in contrast to previous studies that indicated Reelin signaling through PI3K increased cofilin serine3 phosphorylation, stabilizing the actin cytoskeleton in the leading processes of migrating neurons during embryonic mouse brain development (Chai et al., 2009; Frotscher et al., 2017). We posit Reelin's dual role in modulating cofilin activity, either inhibiting or promoting cofilin severing activity, depending on the developmental stage of neurons. Reelin inhibits cofilin severing activity and stabilizes the actin cytoskeleton to act as a stop signal for migrating neurons which is required for orientation and directed migration of cortical neurons (Chai et al., 2009), but it could also function to promote cofilin severing activity by decreasing cofilin serine3 phosphorylation to allow for actin rearrangements essential for neurite outgrowth and arborization in primary murine neuronal cultures.

Reelin is a commanding regulator of neuron growth during different stages of brain development, particularly in embryonic and postnatal stages. Previous studies have shown that dendritic growth of pyramidal cells is disrupted in both homozygous and heterozygous *reeler* mice (Pinto Lord and Caviness, 1979; Niu et al., 2004). Addition of Reelin in vitro has been shown to increase dendritic growth of hippocampal neurons in both WT and *reeler* mutant mice (Niu et al., 2004; Jossin and Goffinet, 2007; Matsuki et al., 2008). This enhancement of dendritic growth by Reelin is evident during early brain development (Nichols and Olson, 2010; Kupferman et al., 2014; Chai et al., 2015; Kohno et al., 2015; O'Dell et al., 2015). Our current study aligns with these findings, focusing on the in vitro effects of Reelin on the dendritic growth and branching of embryonic hippocampal neurons. However, Reelin exerts an opposing effect on dendritic growth in cortical pyramidal neurons and forebrain

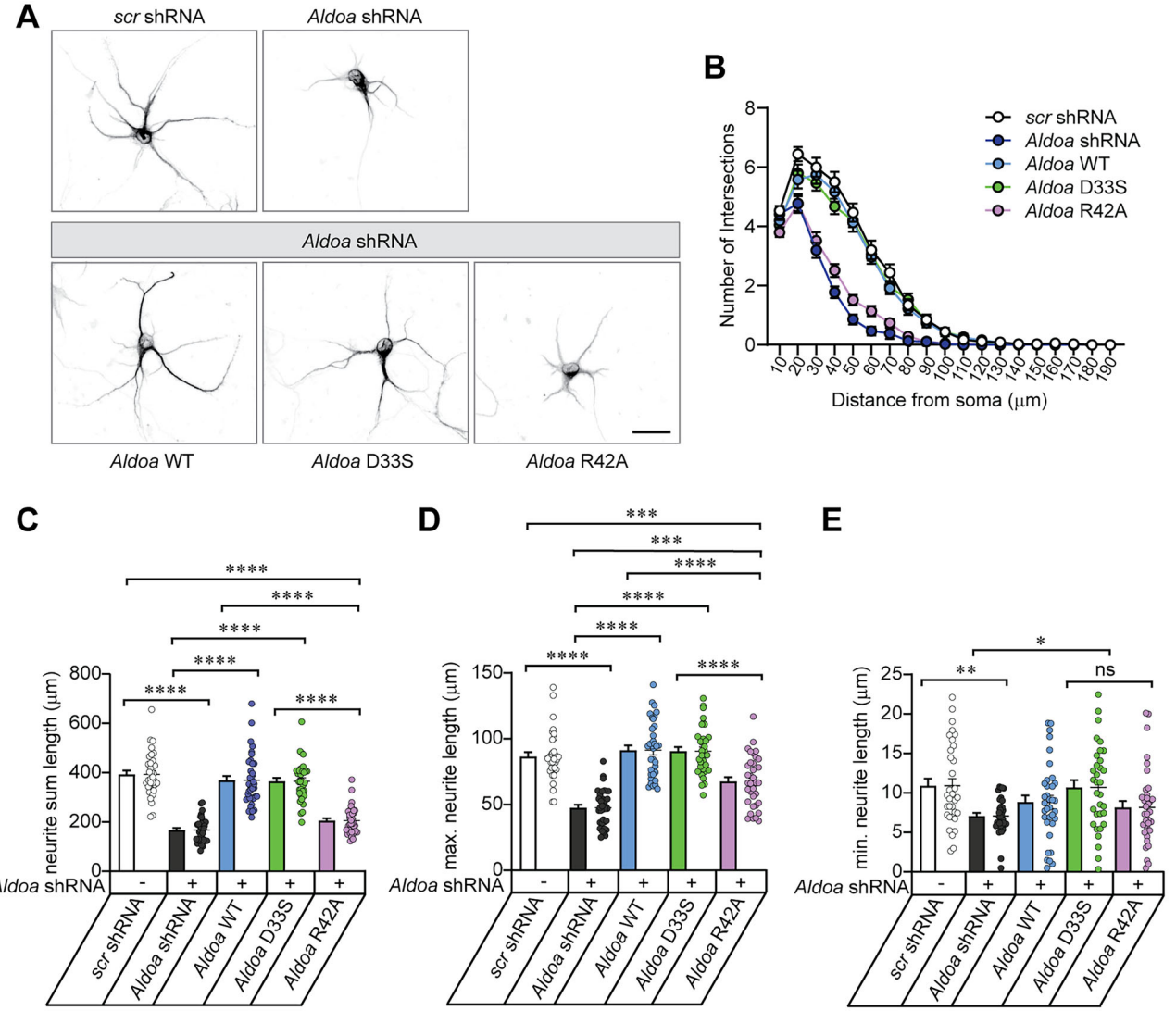

Figure 8. Aldolase A requires actin-binding function to regulate proper neuronal arborization. ***A***, Representative images of DIV 7 neurons immunostained against MAP2 infected with *scr* shRNA, *Aldoa* shRNA, or *Aldoa* shRNA rescue with aldolase A WT, D33S, or R42A variant on DIV1. Scale bar, 25 μm. ***B***, Sholl analysis showed *Aldoa* shRNA-infected neurons exhibit reduced dendritic length and arborization compared with the *scr* control. Lentiviral infection with aldolase WT or D33S variant rescued *Aldoa* shRNA-induced phenotype, while R42A variant was unable to rescue the phenotype. Two-way ANOVA analysis used to determine statistical significance of the interaction between neurite length and number of intersections at each radius for each condition (two-way ANOVA; $F_{(72,\ 3,230)} = 14.70$; $p < 0.0001$). $n = 3$ independent experiments with $n = 34$–36 cells analyzed per condition. ***C***, Bar graph quantification of the average total neurite sum length one-way ANOVA used to determine statistical significance (one-way ANOVA; $F_{(4,\ 170)} = 63.91$; $p < 0.0001$). ***D***, Bar graph quantification of the average maximum neurite sum length (one-way ANOVA; $F_{(4,\ 168)} = 36.06$; $p < 0.0001$). ***E***, Bar graph quantification of the average minimum neurite length (one-way ANOVA; $F_{(4,\ 165)} = 4.176$; $p = 0.003$). For ***C–E***, $n = 3$ independent experiments with $n = 33$–36 neurons analyzed per condition using one-way or two-way ANOVA, Tukey's multiple comparisons. ns, not significant.

interneurons during postnatal development (Yabut et al., 2007; Chameau et al., 2009; Hamad et al., 2021). Specifically, the N-terminal fragment of Reelin has been shown to control and restrict the postnatal maturation of apical dendrites in pyramidal cortical neurons, a process mediated by integrin receptors (Chameau et al., 2009). This suggests that the postnatal effects of Reelin might be attributed to the differential impact of its proteolytic fragments interacting with noncanonical receptors. Our work contributes to the growing body of evidence on the role of Reelin in dendritic development. We provide insights into the proteomic changes through which both canonical and noncanonical Reelin pathways regulate dendrite growth in embryonic cultured neurons at DIV 7. However, it remains unclear whether these in vitro observations fully reflect the in vivo mechanisms and effects of Reelin on dendritic development across various stages of brain maturation. We also recognize that the actin cytoskeletal analysis of this study focuses on the canonical Reelin pathway. Therefore, future studies should examine the contribution of the noncanonical pathway to better understand the effects of actin dynamics in Reelin-induced dendrite growth.

Our proteomics screen identified aldolase A, a glycolytic enzyme and actin-binding protein, as a critical component in Reelin-mediated actin dynamics (Arnold and Pette, 1968; Arnold et al., 1971; Wang et al., 1996; Kusakabe et al., 1997; Jewett and Sibley, 2003). We demonstrated that Reelin stimulates de novo translation of aldolase A, mobilizing soluble aldolase A from the cytoskeleton, linking aldolase A directly to Reelin signaling highlighting a potential role of aldolase A in promoting and stabilizing changes in actin dynamics regulating dendrite development (Fig. 5). We showed that downregulation of aldolase A in primary murine neurons led to shorter, less branched dendrites, and Reelin treatment was ineffective following aldolase

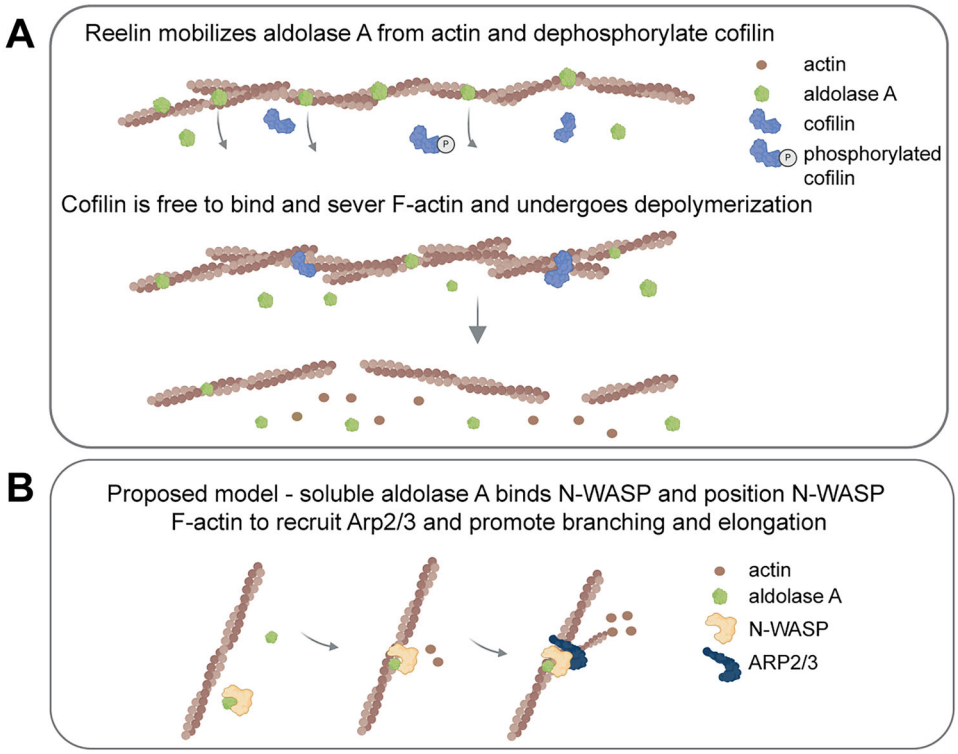

Figure 9. Proposed model in how Reelin affect actin filament-based process during dendrite outgrowth in primary murine neurons. ***A***, Reelin mobilizes aldolase A from actin and dephosphorylates cofilin which promotes cofilin to sever F-actin leading to a decrease in F-actin intensity. ***B***, Testable hypotheses and implications of what increased expression and mobilization of aldolase A might mean in the context of dendritic growth. Increased amount of soluble aldolase A may function to stabilize F-actin and/or promote increased actin branching and elongation through interaction with the N-WASP-Arp2/3 complex, acting as a node to start a new actin branch. The model was created with BioRender.com, Agreement Number BK272QV43D.

A knockdown, indicating aldolase A is necessary for Reelin's effects on dendritic growth. Similar results were observed in cortical neurons in the developing mouse brain, with aberrant length, arborization, and orientation of the apical dendrite (Fig. 7), reinforcing the essential role of aldolase A in proper neuron development.

We further investigated aldolase A's dual functions in neurite outgrowth and demonstrated that the actin-binding ability of aldolase A, rather than its glycolytic function, is critical for neurite development using site-directed variants of aldolase A (Fig. 8). As previously characterized, the D33S aldolase variant is catalytically dead and retains F-actin–binding ability, while the R42A mutant is catalytically active and unable to bind F-actin (Wang et al., 1996; Ritterson Lew and Tolan, 2013; Hu et al., 2016). We demonstrated that both the mouse WT and catalytically inactive D33S aldolase variant, which retains F-actin–binding ability, rescued the effects of *Aldoa* shRNA knockdown phenotype in primary murine neurons, while the R42A mutant, unable to bind F-actin, showed impaired neurite growth and arborization. This finding reinforces aldolase A's role in cell growth and motility, independent of its glycolytic activity, in non-neuronal cells as observed in previous studies (Tochio et al., 2010; Ritterson Lew and Tolan, 2012, 2013; Gizak et al., 2019). Our data establish a direct link between aldolase A and neuronal development downstream of Reelin signaling, revealing a novel functional role for aldolase A in neurons involving actin-binding activity. This expands our understanding of how Reelin might regulate actin filament dynamics, particularly in relation to dendrite growth. Future studies to directly test aldolase A on F-actin dynamics affecting actin remodeling will be important to address.

In summary, our study elucidated how Reelin's canonical and noncanonical signaling pathways influence cytoskeletal development and organization relating to the actin filament-based process during dendrite outgrowth in vitro. Reelin stimulated actin remodeling dynamics by modifying changes in F-actin and β-actin intensity and decreasing n-cofilin phosphorylation. A decrease in n-cofilin phosphorylation likely promotes n-cofilin to sever F-actin, facilitating actin rearrangement. Since previous studies have shown that aldolase A and n-cofilin compete for the same binding site on F-actin (Gizak et al., 2019), we propose a model where Reelin mobilizes aldolase A from the actin cytoskeleton, enabling cofilin-dependent F-actin depolymerization and rearrangement essential for neurite extension and arborization (Fig. 9*A*). However, the implications of increased aldolase A expression and mobilization in the context of dendritic growth are not clear. It is plausible that the increased amount of aldolase A functions to stabilize F-actin and/or promotes increased actin branching through interactions with the N-WASP-Arp2/3 complex which is involved in the nucleation of new actin filaments (Buscaglia et al., 2006; St-Jean et al., 2007). Previous studies have linked aldolase A to Arp2/3-mediated actin polymerization through interactions with WASP in non-neuronal cells (Chiquete-Felix et al., 2009; Ritterson Lew and Tolan, 2013). Given that N-WASP-Arp2/3 complex is also involved in dendrite and dendritic spine formation (Wegner et al., 2008; San Miguel-Ruiz and Letourneau, 2014; Hasegawa et al., 2022), it is possible that dissociated and newly translated aldolase A binds activated WASP and guides it to actin filaments, acting as a node for Arp2/3 to start a new F-actin branch (Fig. 9*B*). Future studies will investigate how Reelin fine-tunes the actin cytoskeleton,

specifically through molecular players like aldolase A, to cooperate and work with other actin-binding proteins in controlling the structure and stability of F-actin networks. Understanding this mechanism will be crucial for understanding how dendrite morphology is shaped.

References

Agnew BJ, Minamide LS, Bamburg JR (1995) Reactivation of phosphorylated actin depolymerizing factor and identification of the regulatory site. J Biol Chem 270:17582–17587.

Arnaud L, Ballif BA, Forster E, Cooper JA (2003) Fyn tyrosine kinase is a critical regulator of disabled-1 during brain development. Curr Biol 13:9–17.

Arnold H, Henning R, Pette D (1971) Quantitative comparison of the binding of various glycolytic enzymes to F-actin and the interaction of aldolase with G-actin. Eur J Biochem 22:121–126.

Arnold H, Pette D (1968) Binding of glycolytic enzymes to structure proteins of the muscle. Eur J Biochem 6:163–171.

Bal M, Leitz J, Reese AL, Ramirez DM, Durakoglugil M, Herz J, Monteggia LM, Kavalali ET (2013) Reelin mobilizes a VAMP7-dependent synaptic vesicle pool and selectively augments spontaneous neurotransmission. Neuron 80:934–946.

Beffert U, et al. (2005) Modulation of synaptic plasticity and memory by Reelin involves differential splicing of the lipoprotein receptor Apoer2. Neuron 47:567–579.

Beffert U, Morfini G, Bock HH, Reyna H, Brady ST, Herz J (2002) Reelin-mediated signaling locally regulates protein kinase B/Akt and glycogen synthase kinase 3beta. J Biol Chem 277:49958–49964.

Bock HH, Herz J (2003) Reelin activates SRC family tyrosine kinases in neurons. Curr Biol 13:18–26.

Bosch C, Muhaisen A, Pujadas L, Soriano E, Martínez A (2016) Reelin exerts structural, biochemical and transcriptional regulation over presynaptic and postsynaptic elements in the adult hippocampus. Front Cell Neurosci 10:138.

Bouche E, Romero-Ortega MI, Henkemeyer M, Catchpole T, Leemhuis J, Frotscher M, May P, Herz J, Bock HH (2013) Reelin induces EphB activation. Cell Res 23:473–490.

Bravo-Cordero JJ, Magalhaes MA, Eddy RJ, Hodgson L, Condeelis J (2013) Functions of cofilin in cell locomotion and invasion. Nat Rev Mol Cell Biol 14:405–415.

Bu G, Rennke S (1996) Receptor-associated protein is a folding chaperone for low density lipoprotein receptor-related protein. J Biol Chem 271:22218–22224.

Buscaglia CA, Penesetti D, Tao M, Nussenzweig V (2006) Characterization of an aldolase-binding site in the Wiskott-Aldrich syndrome protein. J Biol Chem 281:1324–1331.

Carlier MF, Laurent V, Santolini J, Melki R, Didry D, Xia G, Hong Y, Chua NH, Pantolini D (1997) Actin depolymerizing factor (ADF/cofilin) enhances the rate of filament turnover: implication in actin-based motility. J Cell Biol 136:1307–1323.

Caviness VS Jr (1976) Patterns of cell and fiber distribution in the neocortex of the reeler mutant mouse. J Comp Neurol 170:435–447.

Chai X, Fan L, Shao H, Lu X, Zhang W, Li J, Wang J, Chen S, Frotscher M, Zhao S (2015) Reelin induces branching of neurons and radial glial cells during corticogenesis. Cereb Cortex 25:3640–3653.

Chai X, Forster E, Zhao S, Bock HH, Frotscher M (2009) Reelin stabilizes the actin cytoskeleton of neuronal processes by inducing n-cofilin phosphorylation at serine3. J Neurosci 29:288–299.

Chameau P, Inta D, Vitalis T, Monyer H, Wadman WJ, van Hooft JA (2009) The N-terminal region of reelin regulates postnatal dendritic maturation of cortical pyramidal neurons. Proc Natl Acad Sci U S A 106:7227–7232.

Chen Y, Beffert U, Ertunc M, Tang TS, Kavalali ET, Bezprozvanny I, Herz J (2005) Reelin modulates NMDA receptor activity in cortical neurons. J Neurosci 25:8209–8216.

Chen Q, Courtemanche N, Pollard TD (2015) Aip1 promotes actin filament severing by cofilin and regulates constriction of the cytokinetic contractile ring. J Biol Chem 290:2289–2300.

Chiquete-Felix N, Hernandez JM, Mendez JA, Zepeda-Bastida A, Chagolla-Lopez A, Mujica A (2009) In guinea pig sperm, aldolase a forms a complex with actin, WAS, and Arp2/3 that plays a role in actin polymerization. Reproduction 137:669–678.

Curran T, D'Arcangelo G (1998) Role of reelin in the control of brain development. Brain Res Brain Res Rev 26:285–294.

D'Arcangelo G, Miao GG, Chen SC, Soares HD, Morgan JI, Curran T (1995) A protein related to extracellular matrix proteins deleted in the mouse mutant *reeler*. Nature 374:719–723.

Dillon GM, Tyler WA, Omuro KC, Kambouris J, Tyminski C, Henry S, Haydar TF, Beffert U, Ho A (2017) CLASP2 links reelin to the cytoskeleton during neocortical development. Neuron 93:1344–1358.e5.

Dulabon L, Olson EC, Taglienti MG, Eisenhuth S, McGrath B, Walsh CA, Kreidberg JA, Anton ES (2000) Reelin binds a3b1 integrin and inhibits neuronal migration. Neuron 27:33–44.

Frotscher M, Zhao S, Wang S, Chai X (2017) Reelin signaling inactivates cofilin to stabilize the cytoskeleton of migrating cortical neurons. Front Cell Neurosci 11:148.

Gal JS, Morozov YM, Ayoub AE, Chatterjee M, Rakic P, Haydar TF (2006) Molecular and morphological heterogeneity of neural precursors in the mouse neocortical proliferative zones. J Neurosci 26:1045–1056.

Ghosh M, Song X, Mouneimne G, Sidani M, Lawrence DS, Condeelis JS (2004) Cofilin promotes actin polymerization and defines the direction of cell motility. Science 304:743–746.

Gizak A, Wisniewski J, Heron P, Mamczur P, Sygusch J, Rakus D (2019) Targeting a moonlighting function of aldolase induces apoptosis in cancer cells. Cell Death Dis 10:712.

Grayson DR, Jia X, Chen Y, Sharma RP, Mitchell CP, Guidotti AR, Costa E (2005) Reelin promoter hypermethylation in schizophrenia. Proc Natl Acad Sci U S A 102:9341–9346.

Guidotti AR, et al. (2000) Decrease in reelin and glutamic acid decarboxylase$_{67}$ (GAD$_{67}$) expression in schizophrenia and bipolar disorder. Arch Gen Psychiatry 57:1061–1069.

Hamad MIK, et al. (2021) Reelin restricts dendritic growth of interneurons in the neocortex. Development 148:dev199718.

Hasegawa K, Matsui TK, Kondo J, Kuwako KI (2022) N-WASP-Arp2/3 signaling controls multiple steps of dendrite maturation in Purkinje cells in vivo. Development 149:dev201214.

Hiesberger T, Trommsdorff M, Howell B, Goffinet AM, Mumby MC, Cooper JA, Herz J (1999) Direct binding of Reelin to VLDL receptor and ApoE receptor 2 induces tyrosine phosphorylation of disabled-1 and modulates tau phosphorylation. Neuron 24:481–489.

Hong SE, Shugart YY, Huang DT, Shahwan SA, Grant PE, Hourihane JO, Martin NDT, Walsh CA (2000) Autosomal recessive lissencephaly with cerebellar hypoplasia is associated with human RELN mutations. Nat Genet 26:93–96.

Howell BW, Herrick TM, Cooper JA (1999) Reelin-induced tryosine phosphorylation of disabled 1 during neuronal positioning. Genes Dev 13:643–648.

Howell BW, Herrick TM, Hildebrand JD, Zhang Y, Cooper JA (2000) Dab1 tyrosine phosphorylation sites relay positional signals during mouse brain development. Curr Biol 10:877–885.

Hu H, et al. (2016) Phosphoinositide 3-kinase regulates glycolysis through mobilization of aldolase from the actin cytoskeleton. Cell 164:433–446.

Impagnatiello F, et al. (1998) A decrease of reelin expression ass a putative vulnerability factor in schizophrenia. Proc Natl Acad Sci U S A 95:15718–15723.

Jewett TJ, Sibley D (2003) Aldolase forms a bridge between cell surface adhesins and the actin cytoskeleton in apicomplexan parasites. Mol Cell 11:885–894.

Jossin Y (2020) Reelin functions, mechanisms of action and signaling pathways during brain development and maturation. Biomolecules 10:964.

Jossin Y, Goffinet AM (2007) Reelin signals through phosphatidylinositol 3-kinase and Akt to control cortical development and through mTor to regulate dendritic growth. Mol Cell Biol 27:7113–7124.

Kohno T, Honda T, Kubo K, Nakano Y, Tsuchiya A, Murakami T, Banno H, Nakajima K, Hattori M (2015) Importance of Reelin C-terminal region in the development and maintenance of the postnatal cerebral cortex and its regulation by specific proteolysis. J Neurosci 35:4776–4787.

Kohno T, Ishii K, Hirota Y, Honda T, Makino M, Kawasaki T, Nakajima K, Hattori M (2020) Reelin-Nrp1 interaction regulates neocortical dendrite development in a context-specific manner. J Neurosci 40:8248–8261.

Korotkevich G, Sukhov V, Budin N, Shpak B, Artyomov MN, Sergushichev A (2021) Fast gene set enrichment analysis. bioRxiv 060012.

Kupferman JV, Basu J, Russo MJ, Guevarra J, Cheung SK, Siegelbaum SA (2014) Reelin signaling specifies the molecular identity of the pyramidal neuron distal dendritic compartment. Cell 158:1335–1347.

Kusakabe T, Motoki K, Hori K (1997) Mode of interactions of human aldolase isozymes with cytoskeletons1. Arch Biochem Biophys 344:184–193.

Lebherz HG, Rutter WJ (1969) Distribution of fructose diphosphate aldolase variants in biological systems. Biochemistry 8:109–121.
Lee GH, Chhangawala Z, Daake SV, Savas JN, Yates JR, Comoletti D, D'Arcangello G (2014) Reelin induces Erk1/2 signaling in cortical neurons through a non-canonical pathway. J Biol Chem 289:20307–20317.
Leemhuis J, et al. (2010) Reelin signals through apolipoprotein E receptor 2 and Cdc42 to increase growth cone motility and filopodia formation. J Neurosci 30:14759–14772.
Matsuki T, Pramatarova A, Howell BW (2008) Reduction of Crk and CrkL expression blocks reelin-induced dendritogenesis. J Cell Sci 121:1869–1875.
Meijering E, Jacob M, Sarria JCF, Steiner P, Hirling H, Unser M (2004) Design and validation of a tool for neurite tracing and analysis in fluorescence microscopy images. Cytometry 58A:167–176.
Nichols AJ, Olson EC (2010) Reelin promotes neuronal orientation and dendritogenesis during preplate splitting. Cereb Cortex 20:2213–2223.
Niu S, Renfro A, Quattrocchi CC, Sheldon M, D'Arcangelo G (2004) Reelin promotes hippocampal dendrite development through the VLDLR/ApoER2-Dab1 pathway. Neuron 41:71–84.
Niu S, Yabut O, D'Arcangelo G (2008) The Reelin signaling pathway promotes dendritic spine development in hippocampal neurons. J Neurosci 28:10339–10348.
O'Dell RS, Cameron DA, Zipfel WR, Olson EC (2015) Reelin prevents apical neurite retraction during terminal translocation and dendrite initiation. J Neurosci 35:10659–10674.
Pappas GD, Kriho V, Pesold C (2001) Reelin in the extracellular matrix and dendritic spines of the cortex and hippocampus: a comparison between wild type and heterozygous reeler mice by immunoelectron microscopy. J Neurocytol 30:413–425.
Penhoet EE, Kochman M, Rutter WJ (1969) Ioslation of fructose diphosphate aldolases A, B, and C. Biochemistry 8:4391–4395.
Perisco AM, et al. (2001) Reelin gene alleles and haplotypes as a factor predisposing to autistic disorder. Mol Psychiatry 6:150–159.
Pinto-Lord MC, Evrard P, Caviness VS Jr (1982) Obstructed neuronal migration along radial glial fibers in the neocortex of the reeler mouse: a Golgi-EM analysis. Brain Res 256:379–393.
Pinto Lord MC, Caviness VS Jr (1979) Determinants of cell shape and orientation: a comparative Golgi analysis of cell-axon interrelationships in the developing neocortex of normal and reeler mice. J Comp Neurol 187:49–69.
Rice DS, Sheldon M, D'Arcangello G, Nakajima K, Goldowitz D, Curran T (1998) Disabled-1 acts downstream of Reelin in a signaling pathway that controls laminar organization in the mammalian brain. Development 125:3719–3729.
Ritchie ME, Phipson B, Wu D, Hu Y, Law CW, Shi W, Smyth GK (2015) Limma powers differential expression analyses for RNA-sequencing and microarray studies. Nucleic Acids Res 43:e47.
Ritterson Lew C, Tolan DR (2012) Targeting of several glycolytic enzymes using RNA interference reveals aldolase affects cancer cell proliferation through a non-glycolytic mechanism. J Biol Chem 287:42554–42563.
Ritterson Lew C, Tolan DR (2013) Aldolase sequesters WASP and affects WASP/Arp2/3-stimulated actin dynamics. J Cell Biochem 114:1928–1939.
Rogers JT, et al. (2011) Reelin supplementation enhances cognitive ability, synaptic plasticity, and dendritic spine density. Learn Mem 18:558–564.
San Miguel-Ruiz JE, Letourneau PC (2014) The role of Arp2/3 in growth cone actin dynamics and guidance is substrate dependent. J Neurosci 34:5895–5908.
St-Jean M, Izard T, Sygusch J (2007) A hydrophobic pocket in the active site of glycolytic aldolase mediates interactions with Wiskott-Aldrich syndrome protein. J Biol Chem 282:14309–14315.
Sun J, et al. (2021) A novel lncRNA ARST represses glioma progression by inhibiting ALDOA-mediated actin cytoskeleton integrity. J Exp Clin Cancer Res 40:187.
Tissir F, Goffinet AM (2003) Reelin and brain development. Nat Rev Neurosci 4:496–505.
Tochio T, Tanaka H, Nakata S, Hosoya H (2010) Fructose-1,6-bisphosphate aldolase a is involved in HaCaT cell migration by inducing lamellipodia formation. J Dermatol Sci 58:123–129.
Trommsdorff M, Gotthardt M, Stockinger W, Nimpf J, Hammer RE, Richardson JA, Herz J (1999) Reeler/disabled-like disruption of neuronal migration in knockout mice lacking the VLDL receptor and ApoE receptor 2. Cell 97:689–701.
Wang J, Morris AJ, Tolan DR, Pagliaro L (1996) The molecular nature of the F-actin binding activity of aldolase revealed with site-directed mutants. J Biol Chem 271:6861–6865.
Weber CS (1965) *Fructose diphosphate aldolase homologs in embryological development chemistry*. Urbana, Illinois: University of Illinois. pp 198.
Weeber EJ, Beffert U, Jones C, Christian JM, Forster E, Sweatt JD, Herz J (2002) Reelin and ApoE receptors cooperate to enhance hippocampal synaptic plasticity and learning. J Biol Chem 277:39944–39952.
Wegner AM, Nebhan CA, Hu L, Majumdar D, Meier KM, Weaver AM, Webb DJ (2008) N-wasp and the arp2/3 complex are critical regulators of actin in the development of dendritic spines and synapses. J Biol Chem 283:15912–15920.
Willnow TE, Rohlmann A, Horton J, Otani H, Braun JR, Hammer RE, Herz J (1996) RAP, a specialized chaperone, prevents ligand-induced ER retention and degradation of LDL receptor-related endocytic receptors. EMBO J 15:2632–2639.
Yabut O, Renfro A, Niu S, Swann JW, Marín O, D'Arcangelo G (2007) Abnormal laminar position and dendrite development of interneurons in the reeler forebrain. Brain Res 1140:75–83.